

Final
~~Annual~~ Performance Report to the
Air Force Office of Scientific Research (AFOSR)

Ultra-high Capacity Holographic Memories

Georgia Institute of Technology

Principal Investigators:

Ali Adibi

*Associate Professor, School of Electrical and Computer Engineering,
Georgia Institute of Technology
Atlanta, GA 30332-0250
e-mail: adibi@ee.gatech.edu
Tel: (404) 385-2738
Fax: (404) 894-4641*

Faramarz Fekri

*Assistant Professor, School of Electrical and Computer Engineering,
Georgia Institute of Technology
Atlanta, GA 30332-0250
e-mail: fekri@ece.gatech.edu
Tel: (404) 894-3335
Fax: (404) 894-8363*

DISTRIBUTION STATEMENT A
Approved for Public Release
Distribution Unlimited

Steven W. McLaughlin

*Ken Byers Professor, School of Electrical and Computer Engineering,
Georgia Institute of Technology
Atlanta, GA 30332-0250
e-mail: swm@ece.gatech.edu
Tel: (404) 894-6617
Fax: (404) 894-7883*

20050715 018

Part 1: Overview

I. Introduction and Research Accomplishments

This report summarizes the achievements at Georgia Institute of Technology in the area of ultra-high capacity holographic memories funded by Air Force Office of Scientific Research (AFOSR) during the period of December 1, 2001 to October 1, 2004. The primary goal of this research has been to enhance the technologies that will enable the design of ultra-high capacity bulk memories based on the unique properties of volume holographic storage. Such memories have a short access time, a high data transfer rate, and a high storage capacity. In these memories, data is stored in two-dimensional arrays of ones and zeros that are recorded as pages in a holographic material. These data pages can be multiplexed to occupy the same holographic volume. The individual data pages are read by selecting either the angle or the wavelength of the reference beam. Furthermore, the readout from these memories is extremely fast because of the parallelism that is inherent in their large data pages. To take advantage of the advancement in making spatial light modulators with ultra-small pixels, we need to solve the problem of limited spatial bandwidth of the storage material. This limitation puts an upper bound on the smallest pixel size that can be recorded. However, by modulation of the pixel size (while keeping the size above the smallest acceptable value) or modulation of the pixel position using constrained coding, we can improve the number of available bits per page. On the other hand, the data cannot be read out without errors and the bit-error rate varies as a function of the position of the data within the crystal. To get the overall bit-error rate below an acceptable level for bulk storage (less than 10^{-12}) will require error control coding. Maximizing the storage capacity will require optimization of the holographic materials, development of optimized pixel coding using optimized constrained codes, and also the design of optimum two-dimensional error correcting codes that are matched to the noise properties of holographic memories. Therefore, the three main thrusts of the research have been:

- 1) The optimization of holographic storage materials to obtain the best possible combination of the dynamic range, persistence, sensitivity, and dark storage time,
- 2) The development of signal processing techniques and constrained codes to overcome inherent material limitations (such as spatial bandwidth limitation) and increase the number of information bits per page,
- 3) The development of efficient two-dimensional error correcting codes that are optimized for holographic storage. Such codes use the known two-dimensional error patterns in holographic storage to minimize the number of parity bits added for error protection.

While each of these three thrusts has been the major focus of one of the three research teams (lead by A. Adibi, S. McLaughlin, and F. Fekri, respectively) involved in this research, the ultimate goal of the research (i.e., the development of the ultra-high capacity holographic memory system) has been the result of continuous interactions between the three teams.

During the 3-year period of the program, extensive progress has been made in all three thrusts. The development of a complete model for global optimization of doubly-doped photorefractive crystals, especially lithium niobate (LiNbO_3), experimental demonstration of recording high dynamic range and sensitivity in $\text{LiNbO}_3\text{:Fe:Mn}$ crystals, the development of a stabilized holographic read/write setup, the development of a fully two-dimensional low-density parity-check (LDPC) code optimized for holographic memories, and the implementation of new approaches for the incorporation of novel signal processing techniques into holographic memory systems, are the major achievements in this period. Currently, we are in the process of setting up a complete testbed for these volume holographic memory modules. The final goal of the demonstration of a *persistent*

holographic memory system (both hardware and software) for digital data storage for the first time will be achieved in next few months.

II. Publications and Presentations

While several projects are still ongoing and multiple publications in the near future are expected, the research supported by AFOSR has resulted in 6 published (or accepted for publication) journal papers, 4 submitted journal papers (3 more journal papers are currently under preparation), 15 conference presentations, and one invited talk as follows.

II.A. Journal papers

1. O. Momtahan and A. Adibi, "Global optimization of sensitivity and $M/\#$ for two-center holographic recording," *Journal of Optical Society of America B*, vol. 20, pp. 449-461, 2003.
2. H. Pishro-Nik, N. Rahn timer, J. HA, F. Fekri, and A. Adibi, "Low-density parity-check codes for volume holographic memory systems," *Applied Optics*, vol. 42, pp. 861-870, 2003.
3. H. Pishro-Nik, N. Rahn timer, and F. Fekri, "Non-uniform Error Correction Using Low-Density Parity-check codes", accepted with minor revision in *IEEE Transaction on Information Theory*, accepted letter received in Dec. 2004.
4. H. Pishro-Nik and F. Fekri, "Results on punctured low-density parity-check codes and improved iterative decoding techniques", submitted to *IEEE Transaction on Information Theory*, 2003.
5. A. Karbaschi, O. Momtahan, A. Adibi, and B. Javidi, "Optical correlation using localized gated holography," accepted for publication in *Optical Engineering*, acceptance letter received in Feb. 2005.
6. O. Momtahan, G. H. Cadena, and A. Adibi, "Sensitivity variation in two-center holographic recording," submitted to *Optics Letters*.
7. H. Pishro-Nik and F. Fekri "On Decoding of Low-Density Parity-Check Codes Over the Binary Erasure Channel", *IEEE Transaction on Information Theory*, vol. 50, no. 3, pp. 439-454, March 2004.
8. H. Pishro-Nik and F. Fekri, "Irregular Repeat Accumulate Codes for volume holographic memory systems ", *Applied Optics*, Vol. 43 No.27, September 2004.
9. N. Rahn timer, H. Pishro-Nik, and F. Fekri, "Unequal error protection using LDPC codes", submitted to *IEEE Transaction On Communications*, 2004.
10. S. G. Srinivasa and S. W. McLaughlin, "On $(d_1, \infty, d_2, \infty)$ Run Length Limited Arrays: Tiling Algorithms, Capacity Estimates and Coding Schemes," in preparation to be submitted to *IEEE Transactions on Information Theory* by 2004.

II.C. Invited talk

1. A. Adibi, "Novel applications of gated holographic recording," Photonics West Meeting, San Jose, CA, January 2003.

II.B. Conference presentations

1. O. Momtahan and A. Adibi, "Theoretical limits for the performance of two-center holographic recording," Proceedings of SPIE, vol. 4803, presented in SPIE Annual Meeting, Seattle, WA, July 2002.
2. Y.-M. Wu, O. Momtahan and A. Adibi, "A simple approach for modeling photorefractive materials," Proceedings of SPIE, vol. 4803, presented in SPIE Annual Meeting, Seattle, WA, July 2002.
3. O. Momtahan and A. Adibi, "Thermal fixing in two-center holographic recording," OSA Annual Meeting, Orlando, FL, October 2002.
4. A. Karbaschi, O. Momtahan, and A. Adibi, "Optical correlators using localized gated holography," OSA Annual Meeting, Orlando, FL, October 2002.
5. O. Momtahan, A. Karbaschi, and A. Adibi, "Optimization of thermally-fixed localized holograms for novel applications," Optics in the Southeast Meeting, Huntsville, AL, October 2002.
6. O. Momtahan, G. H. Cadena, and A. Adibi, "Stabilized Two-Center Holographic Recording in Highly Doped LiNbO₃ Crystals," accepted to be presented in CLEO 2005, Baltimore MD, May 2005.
7. H. Pishro-Nik, N. Rahnavard, and F. Fekri, "Nonuniform error protection using Low-density parity check codes," 40th Allerton Conference on Communication, Control, and Computing, Monticello, Illinois, October 2002.
8. H. Pishro-Nik, N. Rahnavard, and F. Fekri, "Non-uniform error protection using low-density parity-check codes", Proceeding of the 40th Annual Allerton Conference on Communication, Control, and Computing. Oct. 2002.
9. H. Pishro-Nik, N. Rahnavard, and F. Fekri, "Results on Non-uniform Error Correction Using Low-Density Parity-check codes", IEEE Global Telecommunications Conference, Dec. 2003.
10. H. Pishro-Nik and F. Fekri, "Improved Decoding Algorithms for Low-Density Parity-Check Codes", 3rd international symposium on turbo codes & related topics, France, 2003.

11. S. Srinivasa and S. McLaughlin, "Algorithms for constructing a class of $(1, \infty, d, k)$ RLL codes and estimates of capacity," 2003 Allerton Conference on Computers and Communications, University Illinois, October 2003.
12. N. Rahnavard, H. Pishro-Nik, and F. Fekri, "Unequal error protection using low-density parity check codes", submitted to IEEE 2004 International symposium on Information Theory. N. Rahnavard and F. Fekri, "Unequal error protection using low-density parity check codes", Proc. International Symposium on Information Theory, p. 449, Chicago, IL, June 2004.
13. H. Pishro-Nik and F. Fekri "Application of Irregular Repeat-Accumulate Codes to Holographic Storage Systems", Proc. 38th Annual Conference on Information Sciences and Systems, Princeton, NJ, March 2004, CDROM.
14. S. G. Srinivasa and S. W. McLaughlin, "Enumeration Algorithms for Constructing $(d_1, \infty, d_2, \infty)$ Run Length Limited arrays: Capacity Estimates and Coding schemes," in 2004 IEEE Information Theory Workshop, pp. 141-146, San Antonio October 2004.
15. S. G. Srinivasa and S. W. McLaughlin, "Signal Recovery from Rotational Pixel Misalignment," accepted to IEEE International Conference on Acoustics Speech and Signal Processing, Philadelphia, March 2005.

III. Awards and Recognitions

1. A. Adibi received Space Act Award from NASA for creative development of non-volatile holographic storage in doubly-doped crystals in October 2002.
2. A. Adibi received the Optoelectronics 2003 Outstanding Young Investigator Award from the International Society for Optical Engineering (SPIE) for outstanding work in gated holographic recording in January 2003.
3. O. Momtahan received ECE Graduate Research Assistant Excellence Award, department of electrical and computer engineering, Georgia Institute of Technology, 2005.
4. H. Pishro-Nik received ECE Graduate Research Assistant Excellence Award, department of electrical and computer engineering, Georgia Institute of Technology, 2005.

IV. Structure of the Report

In what follows, we discuss the major research results obtained ONLY in the last 12 months. Results obtained in the first 22 months of the project were summarized in the previous two annual reports.

Part 2: Two-Center Holographic Storage System

Omid Momtahan, Fengtao Wang, Arash Karbaschi and Ali Adibi

Principal Investigator: Ali Adibi

Two-Center Holographic Storage System

I. Introduction

Photorefractive LiNbO_3 crystals are the main candidates for read-write holographic recording systems [1]. Lithium niobate crystals doped with Fe ($\text{LiNbO}_3\text{:Fe}$) have been used for holographic storage systems[1-2]. The main drawback in using singly doped LiNbO_3 crystals such as $\text{LiNbO}_3\text{:Fe}$ is the erasure of the holograms during data retrieval phase. Recently proposed doubly doped LiNbO_3 crystals, such as $\text{LiNbO}_3\text{:Fe:Mn}$, enable recording persistent holograms using two-center holographic recording [3]. The initial reports show that the dynamic range and the sensitivity of doubly doped lithium niobate need to be improved for high capacity and very fast holographic storage applications [4-5].

Recently in this research, we performed a complete theoretical study on the optimization of dynamic range and sensitivity in two-center recording [6]. We found that the maximum achievable $M/\#$ and sensitivity in $\text{LiNbO}_3\text{:Fe:Mn}$ are 2.13 (per mm) and 0.43 cm/J , respectively. However, it was shown that the maximum dynamic range and sensitivity could not be achieved simultaneously. There is always a trade off between the dynamic range and the sensitivity in two-center recording. In the continuation of the study, we designed and grown a $\text{LiNbO}_3\text{:Fe:Mn}$ crystal with a proper set of parameters to achieve high $M/\#$ and high sensitivity.

In this report, we first present a complete material characterization for the designed $\text{LiNbO}_3\text{:Fe:Mn}$ crystal. For recording holograms, we designed and used a software based stabilizer system to reduce all the unwanted vibration and to perform long time recording. The stabilizer was designed and implemented based on LabVIEW software to reduce the cost of the system. We specifically focus on the variation of sensitivity in two-center recording using the stabilized recording system. We also report, for the first time, the electron tunneling effect in two-center recording. We show that the tunneling effect can increase the diffraction efficiency in doubly doped crystals. Then, we report on the holographic memory system we have designed to store digital data in the $\text{LiNbO}_3\text{:Fe:Mn}$ crystal. This is the first demonstration of the non-volatile holographic memory system that provides read/write storage.

In Section II we describe the stabilized recording system. We show that this simple design can make the recording system considerably more stable with accuracy comparable to the best values reported in the literature. In Section III, the experimental measurements for material characterization are presented and the tunneling effect in $\text{LiNbO}_3\text{:Fe:Mn}$ is observed experimentally and explained. The complete variation of sensitivity with recording and sensitizing intensities is summarized in Section IV. The design and implementation of the memory system are presented in Section V. Finally, the conclusion remarks are made in Section VI.

II. Stabilized System for Holographic Recording

A stable setup is one of the most important factors for recording holograms over a long period of time. The effect of any small vibration or movement (in the order of

wavelength) would be of recording a new hologram and partially erasing the old hologram. Although, the shift may be unnoticeable by the eye, it would result in poor diffraction efficiency of the desired hologram. Any mechanical vibration or any perturbation that might cause a change in the optical beam path prevents the recording of strong holograms. This limitation becomes more evident when attempting long recording time for holograms as needed for material characterization in two-center recording. Therefore, an active stabilizer is imperative for this purpose.

Conventionally, hardware based stabilizers have been implemented that provide the excellent stability requirements needed for long time holographic recording [7-9]. However, the cost and experiment dependent properties of these setups are undesirable. We describe a software-based active stabilizer comparable to those in conventional hardware-based setups with lower cost and more flexibility. To achieve this, the entire stabilizer was designed in the LabVIEW software platform, replacing the need for elements such as lock-in amplifiers, function generators, and in some cases, integrators. The benefit of implementing this design in LabVIEW is that most, if not all, signal processing and system control applications may be easily implemented in the software. The holographic setup we propose is based on Mach-Zender Interferometry and is independent of the crystal itself as shown in Fig. 1.

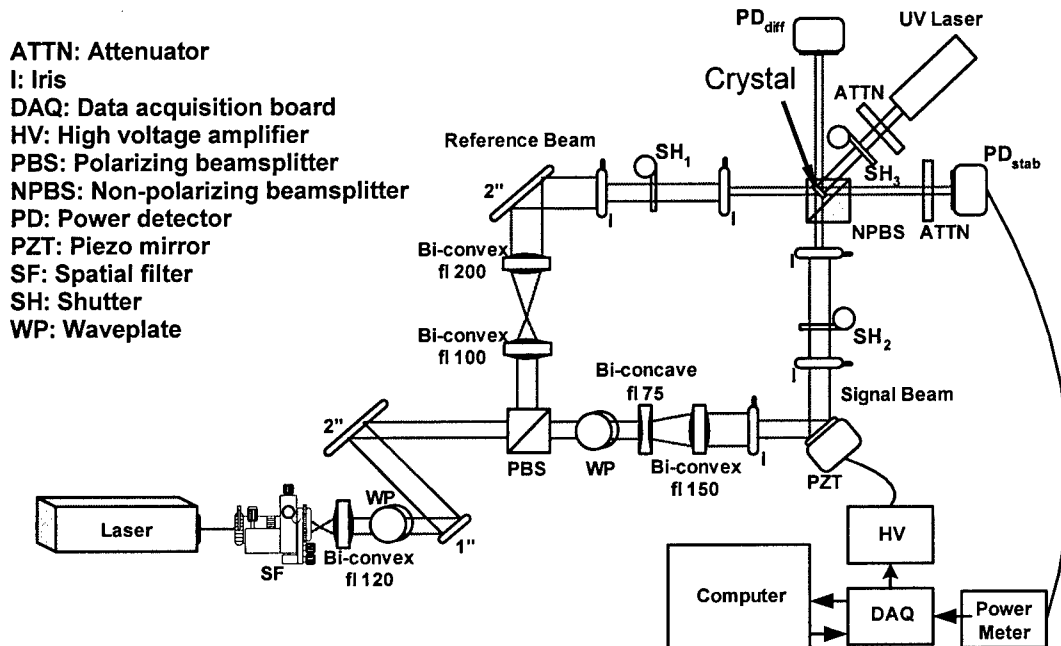


Fig. 1. Stabilized holographic setup.

A continuous-wave solid-state laser generates light at $\lambda = 532\text{-nm}$. The laser beam is spatially filtered, expanded, and collimated. A $\lambda/2$ waveplate (WP) is used to rotate the polarization of the beam properly in order to equally divide the beam power into the signal beam and the reference beam after the beamsplitter. The signal beam is sent through another $\lambda/2$ waveplate to adjust its polarization to match that of the reference beam. The split beams are then expanded to twice their original diameter to encompass

both the crystal and the second (non-polarizing) beam splitter (NPBS). A piezo mirror (PZT) is placed in the path of the object beam. Placing a non-polarizing beamsplitter at the point of intersection of the recording beams causes the two beams to interfere. The interference pattern could be easily observed if a screen is placed after the beamsplitter intersecting the direction of the reference or the signal beam. The crystal was placed on top of the beamsplitter. Extra irises (I) are used to reduce the size of the beam on the crystal while they do not affect the light going into the non-polarizing beamsplitter. A photodetector (PDstab) placed in the reference beam path was adjusted so that it detected the interference of the two beams after the beam splitter. It is this photodetector that monitors the lateral fringe movement. Another photodetector was placed to line up with the signal beam for monitoring the diffracted light intensity. A UV laser beam, at 404 nm, is used to sensitize the crystal. Three shutters (SH) are also used to control the recording-readout process. The fringe movement recorded by PDstab is sent into a power meter and read out through its analog output port. The output of the power meter is taken into the computer via a Data acquisition card (DAQ), processed in LabVIEW, where a phase compensation voltage is determined and sent to a high voltage amplifier which controls the motion of the piezo mirror to lock the fringes of the interference pattern.

Figure 2 show the interference pattern observed in the location of PDstab. A black cardboard having a very small pinhole in the middle covered the photodetector. Therefore, the interference intensity was monitored with sufficient resolution to clearly reveal the fringe movement as shown in Fig. 2.

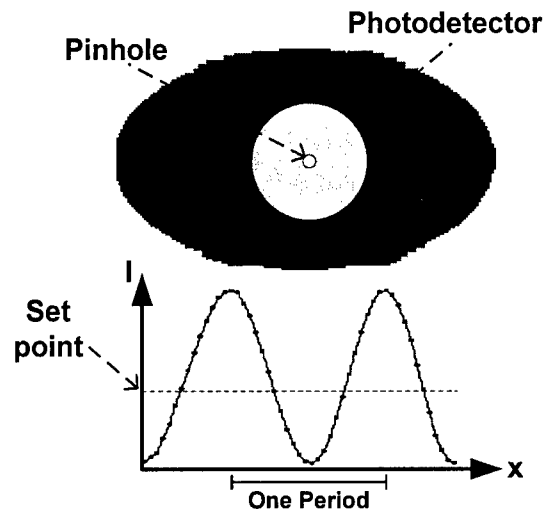


Fig. 2. Fringe movement measurement using a photodetector, covered by thick cover with a pinhole opening. The pinhole is small enough to provide sufficient resolution for measuring the fringe movement.

The stabilization principle of this setup is rather straightforward: an arbitrary set point, corresponding to an arbitrary phase between the interfering beams is chosen as in Fig. 2. A process variable that in our case is the reading from a photodetector, covered by thick cover with a pinhole opening, is subtracted from this set point to produce an error. That error is passed into two PID (proportional, Integral, derivative) controllers that are in

series to compensate for the poles and zeroes of the unstable system and to make a closed loop stable one. The processed error is then passed to a phase shifting element, piezo shifting mirror, which is used to compensate the phase perturbation in the fringe pattern. The PID gains were carefully set to obtain a good stability. The PID controllers are implemented in the software as mentioned before. Figure 3 shows the output of the photodetector (PDstab) for two measurements. In the first measurement, Fig. 3(a), the stabilizer system is off. The measured power is the actual fluctuation in the fringe pattern of the system. In the second measurement, Fig. 3(b), the stabilizer system is active and keeps the system stable around the set point of 10 mW/cm^2 . Comparing these two figures clearly shows the importance of the active stabilizer system. Without that the holographic recording setup would not provide reliable measurements for accurate characterization of doubly doped crystals for two-center recording.

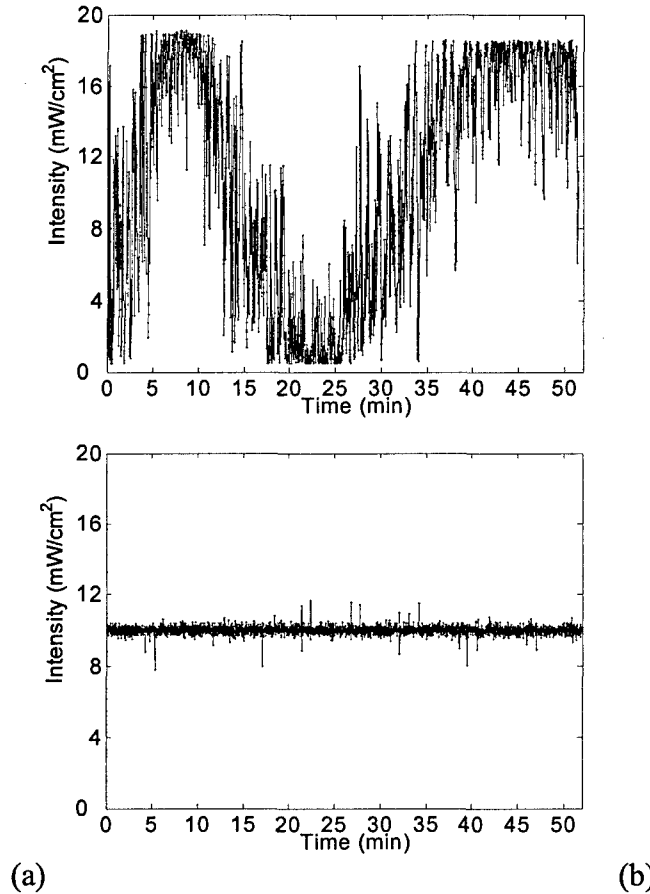


Fig. 3. Intensity monitored by stabilizer photodetector (PDstab) over 50 minutes interval for two cases, (a) without active stabilizer and (b) with active stabilizer.

III. Material Characterization

For material characterization, several holographic experiments with different recording parameters were performed in a 2 mm thick x-cut $\text{LiNbO}_3\text{:Fe:Mn}$ crystal doped with 0.15 wt. % Fe_2O_3 and 0.02 wt. % MnO . The crystal was grown by Deltronics crystals, Inc. These doping concentrations were chosen an extensive optimization effort performed in this research and by considering the trade-off between the $M/\#$ and sensitivity. Initially,

the crystal was heated up to 1200 °C for 12 hours in Oxygen environment to ensure all the Fe traps were empty and a portion of the Mn traps were filled. Each hologram was recorded in the presence of a sensitizing beam ($\lambda = 404$ nm) using two green ($\lambda = 532$ nm) plane-waves with equal power. The holograms were recorded in transmission geometry and the total angle between the two recording beams in the air was 90°. The power of the two recording beams was set to be equal to get the maximum possible index modulation. The polarization of the recording beams was ordinary. In all the experiments the diffraction efficiency is calculated as the ratio of the diffracted power to the total incident power of the reading beam.

Figure 4 shows the diffraction efficiency for a hologram recorded for 30 minutes and immediately read for 3 hours. Total recording intensity and the sensitizing intensity are 23 mW/cm² and 10 mW/cm², respectively. Before the recording phase, the hologram is sensitized with the sensitizing beam (Intensity 10 mW/cm²) for 1 hour. After recording, the hologram was illuminated by a Bragg mismatched beam at $\lambda = 532$ nm with the same intensity as one of the recording beams. As seen in Fig. 4, the dynamic of the recording phase is exactly similar to the other recording dynamics reported in the literature [3-6]. However, the readout portion of the curve shows a new behavior not being observed in other reports. As it is seen in Fig. 4, the diffraction efficiency does not decrease at the beginning of the readout. Instead, the diffraction efficiency increases first and then decrease. To reduce the experimental uncertainty, the experiment was repeated several times and the same behavior was observed in all trials.

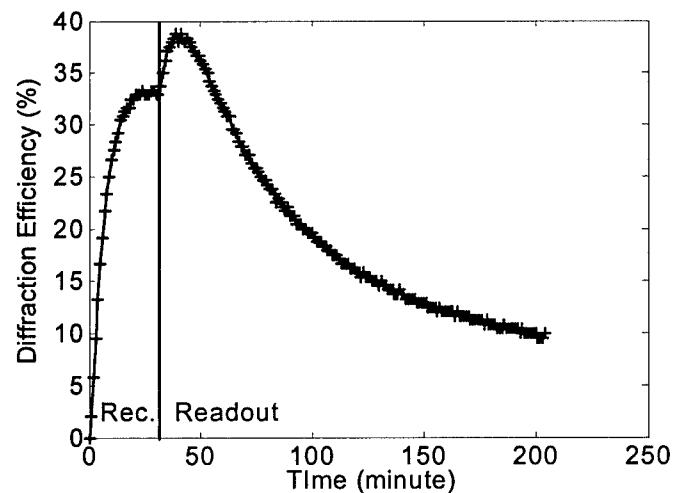


Fig. 4. Recording-readout curve for LiNbO₃:Fe:Mn doped with 0.15 wt. % Fe₂O₃ and 0.02 wt. % MnO. A 2 mm thick sample is used. The sensitizing and recording wavelengths are 404 nm and 532 nm, respectively. Sensitizing intensity and the total recording intensity are 10 mW/cm² and 23 mW/cm², respectively. The polarization of the recording beams is ordinary. Readout is performed while the crystal is illuminated using a Bragg mismatched green ($\lambda = 532$ nm) beam with an intensity of 10 mW/cm². The total angle between the recording beams outside the crystal is 90° in transmission geometry. The recording to sensitizing intensity ratio is 2.3. Recording time is 30 minutes.

To investigate the behavior, a new set of experiments was performed. In each experiment the hologram was recorded as describe before. After the recording phase, the hologram was kept in the dark and the diffraction efficiency was monitored from time to time using a weak reading beam. Total exposure of the reading beam was kept very small to

minimize the possible effects on the hologram. After this phase, the hologram was read in the presence of a Bragg-mismatched beam to observe the partial erasure of the hologram. Figure 5 shows the results for the recoding experiment for 30 minutes followed by dark monitoring for 150 minutes. The readout was performed after the dark monitoring phase for another 150 minutes. As it is seen in Fig. 5, the diffraction efficiency keeps increasing even after the recording while being in the dark without any external light illumination.

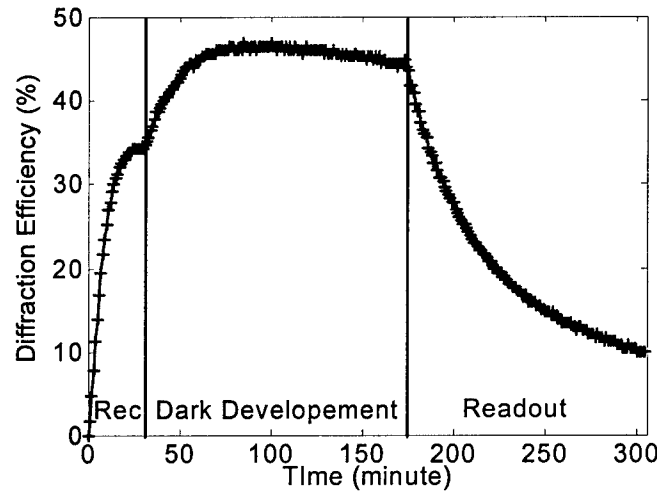


Fig. 5. Recording-dark development-readout curve for $\text{LiNbO}_3\text{:Fe:Mn}$ doped with 0.15 wt. % Fe_2O_3 and 0.02 wt. % MnO . After the recording phase the crystal is kept in the dark while the diffraction efficiency is monitored from time to time. All other parameters are the same as those in the caption of Fig. 4.

The increase in the diffraction efficiency after the recording phase can be explained as follows. The $\text{LiNbO}_3\text{:Fe:Mn}$ crystal used in the experiments has a high concentration of Fe traps (0.15 wt. %). From singly doped lithium niobate crystals such as $\text{LiNbO}_3\text{:Fe}$, we know that there are two mechanisms of dark decay of the hologram strength [10-12]. The first one, that is called the ionic dark decay, is due to compensation of the electron distribution by the protons (H^+). The rate of ionic dark decay increases with the increase in the temperature. This proton compensation is the main effect that is used for thermal fixing in elevated temperatures [12]. The other mechanism is called electronic dark decay. The major cause of this phenomenon is believed to be the electron tunneling between sites of Fe^{2+} and Fe^{3+} in the crystal [10-11]. The dominant mechanism of the dark decay at room temperature in lithium niobate doped with more than 0.05 wt % Fe is the electron tunneling [10-11].

In the doubly doped crystal used for our experiments, Fe concentration is very high while the Mn concentration is relatively low. Based on the results in singly doped crystals, the tunneling effect can be an important factor for compensating the electronic distribution in the Fe sites. We also know that the modulated electronic distributions in the Fe and Mn traps are almost equal but with 180° phase shift with respect to each other [4]. Therefore, the tunneling between the Fe sites reduces the modulated Fe concentration, and thus increases the total modulated concentration of electrons. Since the electric field is proportional to the total modulated charge concentration, it increases with tunneling and results in increase in the diffraction efficiency as observed in Fig. 5. This effect is

observed by our team for the first time in two-center holographic recording. The importance of the tunneling effect in two-center recording is the increase in the diffraction efficiency in contrast to decrease of that in one-center recording. Considering the tunneling effect and designing a proper set of parameters for the crystal can result in a better performance compared to the usual two-center recording.

IV. Variation of Sensitivity in Two-Center Recording

In two-center recording, besides the recording beams, a sensitizing beam should be used to record a hologram. Therefore, the sensitizing beam may provide another parameter of control for recording in doubly doped crystals. It was reported both experimentally and theoretically that $M/\#$ in two-center recording is a function of the ratio of the recording to sensitizing intensity and not the absolute intensities [4]. Therefore, the sensitizing intensity is not an independent parameter for $M/\#$ in two-center recording. Instead, it is combined the recording intensity to form an important parameter, the ratio of recording to sensitizing intensities, for $M/\#$ in two-center recording.

In this research we showed theoretically, for the first time, that sensitivity also depends on the ratio between total recording intensity and sensitizing intensity (I_{rec} and I_{sen} , respectively) and not on the absolute intensities [6]. In this section, we report for the first time, a detailed experimental study of the role of recording and sensitizing intensities in two-center recording. We show that the sensitivity depends only on the intensity ratio (i.e., I_{rec}/I_{sen}) and not on the individual intensities as predicted theoretically [6].

All experiments reported in this section were performed using a modified stabilized recording system as shown in Fig. 6.

The crystal used for the experiments is the same as that used in previous experiments. To study the variation of the sensitivity in two-center recording, different holograms were recorded using different sets of recording and sensitizing intensities. Before any experiment, the crystal was illuminated by the UV beam to erase the existing holograms. Then, a two-center hologram is recorded to saturation for a long time (1 hour or more) using two beams (shown by dashed lines in Fig. 6), which are Bragg-mismatched with the reference and signal beams of the desired hologram. This process is added to obtain a steady state electron concentration in the Fe and the Mn traps before recording the desired hologram in order to have a reliable measurement of the sensitivity. Then, the desired hologram is recorded using the reference and signal beams as shown in Fig. 6 for at least 3 minutes and the diffraction efficiency is monitored in 30 seconds intervals. After each recording, the hologram was illuminated by the two Bragg-mismatched beams (shown by dashed lines in Fig. 6) and the sensitizing beam for at least 30 minutes to erase the previous hologram before recording the next desired hologram while the average electron concentrations in the two traps were kept at their steady-state value during recording. For each set of recording and sensitizing intensities, the same experiment was repeated at least four times and the recording time in the forth experiment was chosen long enough to make sure the hologram reached the saturation. The hologram was then illuminated using one of the Bragg-mismatched beams to partially erase the hologram and to find the persistent diffraction efficiency.

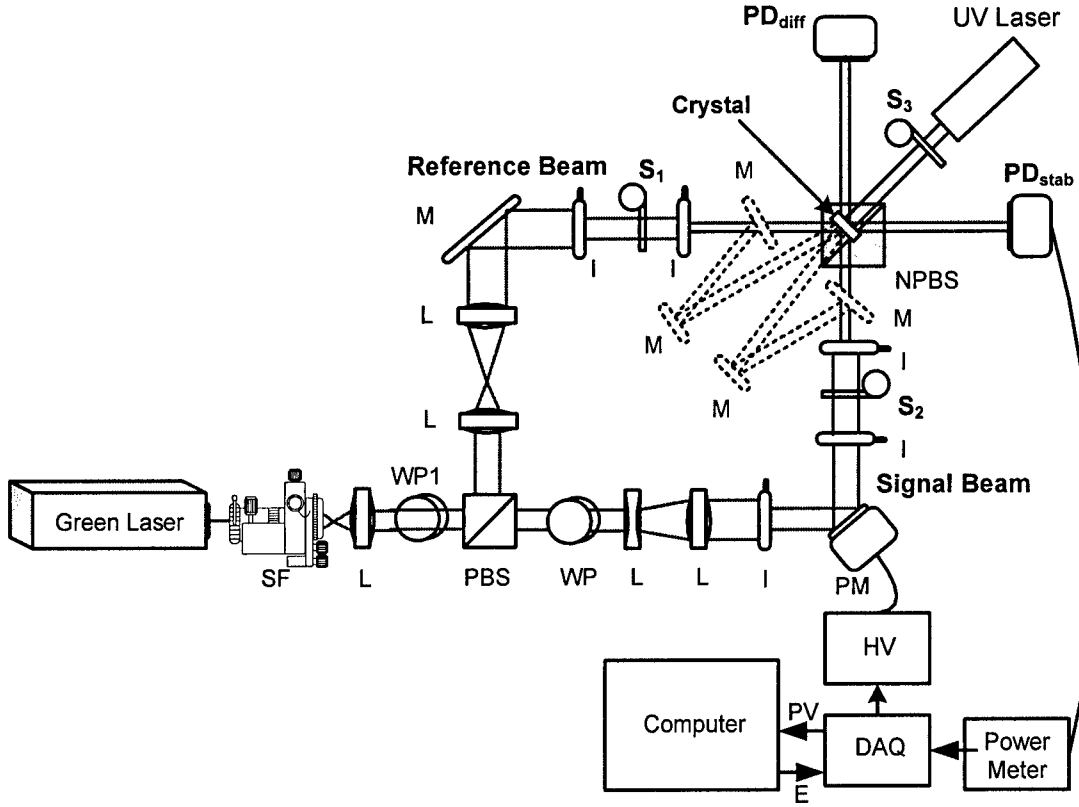


Fig. 6. Recording setup used for sensitivity measurement. The setup in Fig. 1 was slightly changed by adding two flipper mirrors and two fixed mirrors (shown by dashed lines) to provide two Bragg-mismatched beams. DAQ, data acquisition card; HV, high voltage amplifier; I, iris; L, lens; M, mirror; NPBS, non-polarizing beam splitter; PBS, polarizing beam splitter; PD, power detector; PZT, piezo mirror; S, shutter; SF, spatial filter; WP: half waveplate.

The sensitivity (S) is then calculated as [13]

$$S = \frac{1}{I_{rec}L} \times \left. \frac{d\sqrt{\eta}}{dt} \right|_{t=0}, \quad (1)$$

where η , t , I_{rec} , and L represent diffraction efficiency (ratio of diffracted intensity to incident reading intensity), time, total recording intensity (sum of the intensities of the two recording beams), and the crystal thickness, respectively. The persistent sensitivity in two-center recording is defined as [14]

$$S' = S\beta = \frac{\beta}{I_{rec}L} \times \left. \frac{d\sqrt{\eta}}{dt} \right|_{t=0}, \quad (2)$$

where β is the ratio of $\sqrt{\eta}$ after sufficient readout to $\sqrt{\eta}$ at the end of recording (before any readout). The values of S and S' were calculated for all four experiments and then averaged to find the sensitivity for each set of intensities.

Figure 7 shows the variation of S with the recording intensity when the ratio of the recording and sensitizing intensities is kept constant at $I_{rec}/I_{sen} = 3.1$. As it is seen in Fig. 7, the sensitivity is almost constant for a fixed intensity ratio, as predicted from the theoretical analysis [6]. Therefore, to obtain the complete variation of sensitivity with respect to recording and sensitizing intensities, we only need to find S (or S') as a function of I_{rec}/I_{sen} .

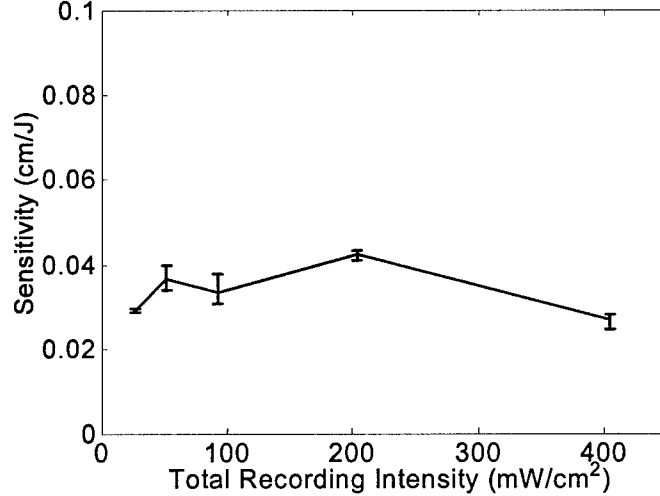


Fig. 7. Sensitivity (S) in two-center recording as a function of total recording intensity (I_{rec}) while the recording to sensitizing intensity ratio is fixed at $I_{rec}/I_{sen} = 3.1$. The properties of the $\text{LiNbO}_3\text{:Fe:Mn}$ crystal is summarized in the caption of Fig. 4. The sensitivity and recording wavelength are 404 nm and 532 nm, respectively.

The variation of sensitivity (S) with I_{rec}/I_{sen} is shown in Fig. 8. From Fig. 8 it is clear that S decreases as the intensity ratio increases as we had theoretically predicted in Ref. [6]. Another important result is that the maximum sensitivity (S), which is 0.15 cm/J, is obtained with the intensity ratio of $I_{rec}/I_{sen} = 0.54$. This suggests that for achieving high sensitivity, we need to use a sensitizing beam with higher intensity compared to the recording intensities.

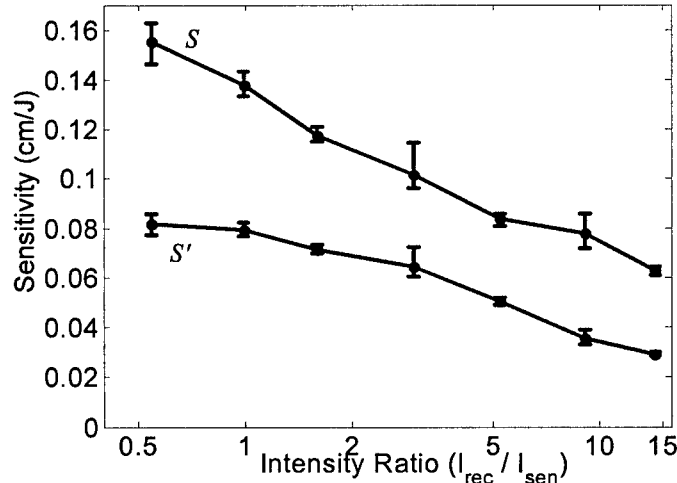


Fig. 8. Sensitivity in two-center recording as a function of as a function of that ratio of recording to sensitizing intensities (I_{rec}/I_{sen}). The persistent sensitivity (S') is equal to $\beta \cdot S$.

The variation of persistent sensitivity (S') with I_{rec}/I_{sen} is also shown in Fig. 8. As it is clear in this figure, although smaller intensity ratios result in higher values for S , the sensitivity corresponding to persistent hologram (S') reaches its maximum value of 0.08 cm/J around the intensity ratio of 0.54. Further decrease of the intensity ratio will result in the reduction of S' . On the other hand, for the high intensity ratios, the difference between S and S' becomes smaller and smaller because of larger values of β at higher I_{rec}/I_{sen} . The variation of S' with the ratio of recording to sensitizing intensities is in good agreement with our theoretical results [6]. Note that, the thickness of the crystal used for the measurement was 2 mm. Because of high absorption of the crystal, the sensitizing beam intensity drops rapidly and only a small thickness of the crystal can observe the optimum ratio of the recording to sensitizing intensity [6]. Using a thinner crystal, or sensitizing from both sides of the crystal, we can obtain higher values for sensitivity ($S \approx 0.3$ cm/J). Also, using extraordinary polarization for the reading beams results in another factor 3 improvement in S (*i.e.*, $S \approx 1$ cm/J). Nevertheless, the sensitivity obtained by us in this research $S = 0.15$ cm/J is the highest reported ever for LiNbO₃:Fe:Mn.

V. Two-Center Holographic Memory System

The LiNbO₃:Fe:Mn crystal we have designed and tested is used to realize the actual high capacity memory system that provides persistent read/write storage. The Fourier transform holograms are recorded in a $1 \times 1 \times 1$ cm³ crystal using recording beams at $\lambda = 532$ nm and a sensitizing beam at $\lambda = 404$ nm. The holographic memory setup is shown in Fig. 9. The light from a solid-state laser is spatially filtered, collimated and then divided into signal and reference beams using a polarizing beam splitter (PBS). A half wave plate (WP) at 532 nm wavelength is placed before PBS to control the ratio of the reference intensity to the signal intensity. The signal beam passes through a spatial light modulator (SLM), which modulates the amplitude of the signal beam. Right after the SLM, we placed a polarizer (P) to let the proper polarization, parallel to the reference beam, propagate. The SLM has 1024×768 pixels each having a size of $14 \mu\text{m} \times 14 \mu\text{m}$. The signal then propagates through a $4f$ system, consisting of two Fourier transforming lens (FLs). The crystal is placed in the middle of the $4f$ system at the Fourier plane of the first lens. The holograms are recorded in Fourier domain to efficiently use the material [1]. Also, the Fourier transform holograms are less sensitive to the imperfection of the material. The recording geometry in this setup is 90-degree geometry to obtain high capacity [1].

The reference beam is reflected using a rotating mirror (RM) and then passes through the $4f$ system. The $4f$ system is used to provide the rotation of the reference beam while its location on the crystal is fixed. The holograms are multiplexed in the crystal using angular multiplexing [1]. After recording each hologram, the RM is rotated for 0.02° to record the next hologram. The angular separation of 0.02° (measured in the air) is about four times the angular selectivity of the hologram and ensures very low crosstalk between the adjacent holograms. The angle of the reference beam for recording each hologram is stored as the address of the corresponding data page. To read one of the holograms, the RM is rotated to the angular address of that hologram and the diffracted beam is monitored using the CCD as shown in Fig. 9.

For recording two-center holograms the crystal should be sensitized with a UV beam at 404 nm during recoding. The sensitizing section of the setup is shown with dashed lines in Fig. 9 and the details of it are shown in Fig. 10. The beam from a UV laser is first expanded and split using a non-polarizing beam splitter (NPBS). The two sensitizing beams illuminate the crystal with oblique angles (20° incident angle measured in the air) from the direction of the signal beam. This arrangement is used to symmetrically sensitize the crystal with respect to the signal beam. During the recording three computer-controlled shutters are used to block the signal, reference and sensitizing beams, respectively (not shown in Fig. 9). The computer is also used to control the rotation of the RM, to provide the angular address information for different holograms, and to display the desired data page on the SLM during the recording. Also, the diffracted beam from the crystal in the readout phase is captured by the CCD and stored in the computer for decoding and further processing. The picture of the actual system is shown in Fig. 11.

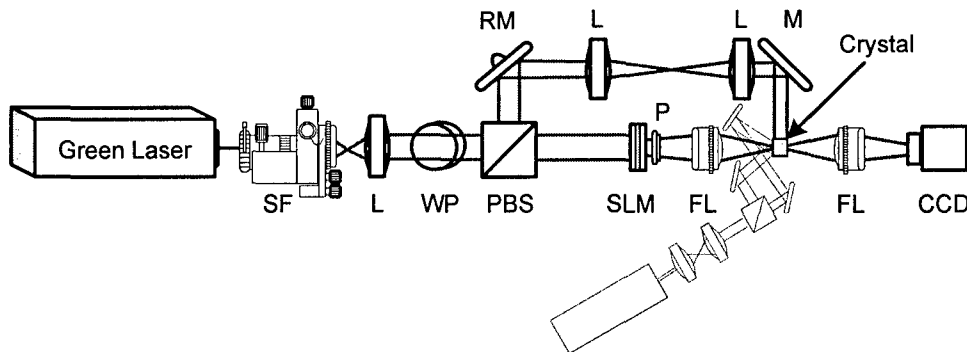


Fig. 9. Holographic setup used for storage application. SF, spatial filter; WP, half waveplate; PBS, polarizing beam splitter; L, lens; FL, Fourier transforming lens; M, mirror; RM, rotating mirror; SLM, spatial light modulator; P, polarizer; CCD, charge-coupled device (camera).

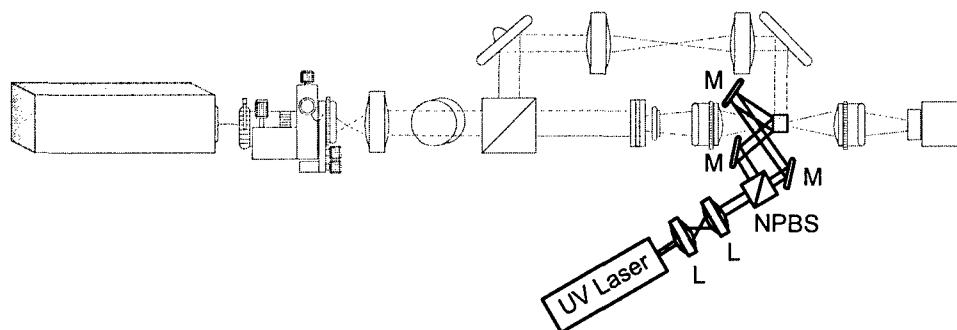


Fig. 10. The sensitizing part of the holographic storage system. L, lens; NPBS, non-polarizing beam splitter; M, mirror.

The main challenge for the memory system is to image each pixel of the SLM to each pixel of the CCD using the $4f$ imaging system, often called pixel matching. Considering the $14\ \mu\text{m} \times 14\ \mu\text{m}$ pixels of the SLM and $6.7\ \mu\text{m} \times 6.7\ \mu\text{m}$ pixels of the CCD, the imaging system should have demagnification ratio of 0.48. Also, the imaging system should be able to pass high frequency components of any image formed on the SLM. For example, the lens should be able to resolve two pixels separated $28\ \mu\text{m}$ on the SLM corresponding to the highest spatial frequency of the imaging system. The point-spread

function (defined as the image of a point source in an imaging systems [15]) of the practical lenses has a finite width. It means that a practical lens blurs the small feature sizes of the object through the imaging. Therefore, the point spread function of the first lens used for the $4f$ imaging system for the signal beam (FL in Fig. 9) should be narrower than $28\text{ }\mu\text{m}$ in the current arrangement in order to fully resolve the patterns on the SLM. The same limitation imposed by the pixel size of the CCD holds for the second lens in the $4f$ imaging system (also shown by FL in Fig. 9).

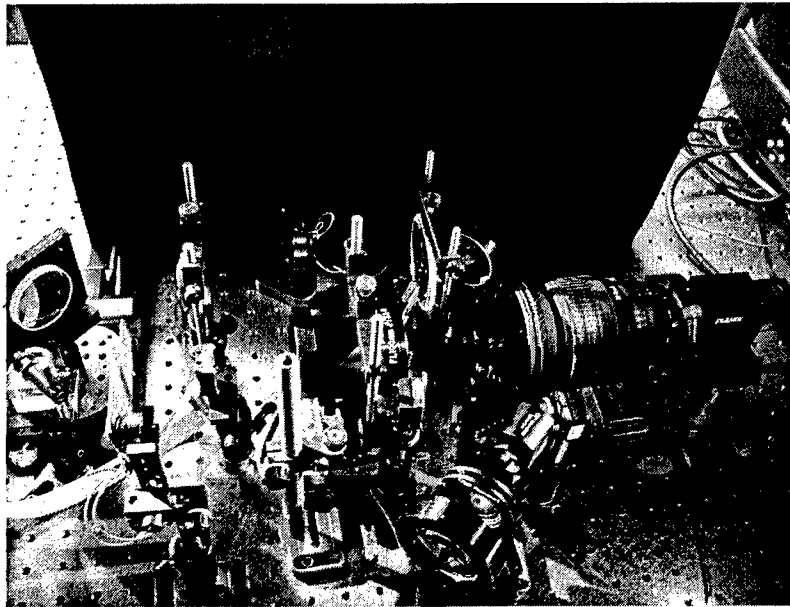


Fig. 11. The picture of the actual holographic storage setup.

It should be noted that the pixel sizes for SLM and CCD used in this work are among the smallest pixel sizes ever used in a pixel matching system. This makes the design of the $4f$ imaging system very complicated. We have been able to achieve pixel matching for pixels with the lowest size of $28\text{ }\mu\text{m} \times 28\text{ }\mu\text{m}$ on the SLM. It means that a group of 2 by 2 pixels ($28\text{ }\mu\text{m} \times 28\text{ }\mu\text{m}$) on SLM is completely matched with a group of 2×2 pixels ($13.4\text{ }\mu\text{m} \times 13.4\text{ }\mu\text{m}$) on the CCD. Currently, we are developing and testing a new $4f$ imaging system is designed and being tested to obtain the pixel matching for very small pixel size of as low as $10\text{ }\mu\text{m} \times 10\text{ }\mu\text{m}$.

VI. Summary and Conclusion

The $\text{LiNbO}_3\text{:Fe:Mn}$ crystal, which had been designed for optimum performance, was characterized using a software based stabilized holographic system. The stabilizer system was based on Mach-Zender interferometry and was implemented using LabView software to reduce the cost of the system. Using this system, we were able to achieve the stability better than $\lambda/20$ (recording wavelength $\lambda = 532\text{ nm}$) for intervals of at least two hours.

In the characterization of the material we observed and explained, for the first time, the tunneling effect in two-center recording. Since the concentration of Fe is very high (0.15 wt %) in the crystal, the electron can tunnel between the Fe sites resulting in the erasure

of the modulated electron concentration (or the hologram recorded) in the Fe traps. On the other hand, the tunneling does not affect the electron distribution in the Mn traps. Since the modulated electronic distributions in the Fe and Mn traps are almost equal but with 180° phase shift with respect to each other, erasing the modulated concentration in the Fe traps results in the increase of the total modulated electron concentration and, therefore, the higher diffraction efficiency. In contrast to singly doped crystals in which tunneling erases the recorded hologram and reduces the diffraction efficiency, tunneling in doubly doped crystals can increase the diffraction efficiency. The tunneling effect can be used to enhance the performance of the two-center recording.

The complete variation of sensitivity in two-center recording as a function of recording and sensitizing intensities is obtained experimentally that is in good agreement with the theoretical predictions. It is shown that the sensitivity in two-center recording is a function of the ratio of the recording to sensitizing intensities and not the absolute intensities. Also, in recording at 532 nm wavelength and sensitizing at 404 nm wavelength, using high intensity UV sources is a key factor for fast recording in doubly doped crystals. It is found that the sensitivities up to 0.3 cm/J can be obtained using this crystal. The sensitivity obtained in our optimal crystal is the highest reported to date for $\text{LiNbO}_3\text{:Fe:Mn}$.

The holographic memory system is designed and set up for persistent holographic storage. With 1000 holograms multiplexed in a 1 cm^3 crystal, we can achieve memory module with 1 Gb capacity. The setup is the first demonstration of non-volatile and rewritable holographic memory system. The system was tested for recording data pages up to 200 Kbit of data. Currently, the system is being improved to be capable of recording data pages up to 1 Mbits of data.

VII. Reference

1. H. J. Coufal, D. Psaltis, G. T. Sincerbox (Eds.), *Holographic Data Storage*, (Springer, Berlin, 2000).
2. J. Ashley, M. P. Bernal, G. W. Burr, H. Coufal, H. Guenther, J. A. Hoffnagle, C. M. Jefferson, B. Marcus, R. M. Macfarlane, R. M. Shelby, G. T. Sincerbox, "Holographic data storage," *IBM J. Res. Dev.* 44, pp. 341-368 (2000).
3. K. Buse, A. Adibi, and D. Psaltis, "Non-volatile holographic recording in doubly doped lithium niobate crystals," *Nature* 393, pp. 665-668 (1998).
4. A. Adibi, K. Buse, and D. Psaltis, "Two-center holographic recording," *J. Opt. Soc. Am. B* 18, 584-601 (2001).
5. Y. W. Liu, L. R. Liu, Y. C. Guo, and C. H. Zhou, "The dynamics of holographic storage in doubly doped $\text{LiNbO}_3\text{:Fe:Mn}$," *Acta Physica Sinica* 49, 880-886 (2000).
6. O. Momtahan, and A. Adibi, "Global optimization of sensitivity and dynamic range for two-center holographic recording," *J. Opt. Soc. Am. B*, vol. 20, pp. 449-461 (2003).
7. D. B. Neumann and H. W. Rose, "Improvement of recorded holographic fringes by feedback control," *Appl. Opt.* 6, pp. 1097-1104 (1967).

8. D. R. MacQuigg, "Hologram Fringe Stabilization Method," *Appl. Opt.* 16, pp. 291-292 (1977).
9. K. Peithmann, A. Wiebrock, and K. Buse, "Incremental holographic recording in lithium niobate with active phase locking," *Opt. Lett.* 23, pp. 1927-1929 (1998).
10. I. Nee, M. Muller, K. Buse, and E. Kratzig, "Role of iron in lithium-niobate crystals for the dark-storage time of holograms," *J. of Appl. Phys.* 88, pp. 4282-4286 (2000).
11. Y.P. Yang, I. Nee, K. Buse, and D. Psaltis, "Ionic and electronic dark decay of holograms in $\text{LiNbO}_3 : \text{Fe}$ crystals," *Appl. Phys. Lett.* 78, pp. 4076-4078 (2001).
12. K. Buse, S. Breer, K. Peithmann, S. Kapphan, M. Gao, and E. Kratzig, "Origin of thermal fixing in photorefractive lithium niobate crystals," *Phys. Rev. B*, vol. 56, pp. 1225-1235, July 15, 1997.
13. P. Gunter and J.-P. Huignard, eds., *Photorefractive Materials and Their Applications I*, Vol. 61 of *Topics in Applied Physics* (Springer-Verlag, Berlin, 1987).
14. A. Adibi, K. Buse, and D. Psaltis, "Sensitivity improvement in two-center holographic recording," *Opt. Lett.* 25, 539-541 (2000).
15. J. W. Goodman, *Introduction to Fourier Optics*, 2nd ed. (McGraw-Hill, New York, 1996).

Part 3: Error Control Coding for Volume Holographic Memory Systems

Nazanin Rahnavard, Hossein Pishro-Nik, Faramarz Fekri and Ali Adibi

Principal Investigator: Faramarz Fekri

Error Control Coding for Volume Holographic Memory Systems

Summary

In this project, we investigated the application of error control coding in volume holographic memory (VHM) systems. Recently, low-density parity-check (LDPC) codes have attracted lots of attention because of their good performance and their low complex decoding algorithm that is called message passing. The application of the LDPC codes on VHM systems is a new research problem because of the non-uniform distribution of the noise in a holographic page. In our research, we first introduced a design methodology to construct good LDPC codes for VHM systems that have non-uniform error pattern. We showed that these codes have superior performance to Reed-Solomon (RS) Codes. Our simulation showed that we increased the storage capacity of holographic memories by more than 50 percent by using irregular LDPC codes instead of RS codes. The performance of these LDPC codes is close to the information theoretic capacity.

Although LDPC codes have a low complex decoding algorithm, their encoding complexity is quadratic in the code length. To overcome this problem we next applied another type of codes that are called Turbo-like codes or Repeat-Accumulate (RA) codes. These codes are special case of LDPC codes with low encoding complexity. This makes them very good candidates for VHM systems that fast encoding and decoding is very important. More importantly, since VHM systems require very small error rates, we gave an RA code design that avoids error floor effect.

1. ECC for VHM Systems

Storage capacity of a VHM system is defined as the number of information bits stored under the condition that BER is lower than required value. The information theoretic capacity is the highest theoretically achievable capacity. Since the diffraction efficiency of the recorded holograms decreases with increasing the number of pages, BER increases when we increase the number of stored pages. To increase the storage capacity, we can store more pages and use ECC to decrease BER to the desired value. If we increase the number of stored pages by a factor f , the capacity of the system is increased

by the factor $f \times R$, where R is the code rate (the ratio of the number of information bits to the total number of bits). Thus, for a constant number of pages, in order to have the highest storage capacity we need to find a code with highest rate that provides us with the required output BER.

2. LDPC Codes for VHM Systems

The application of capacity achieving codes for these systems was introduced in [1]. Using capacity achieving codes we can obtain the highest storage capacity for VHM systems. In [1], we proposed LDPC codes for VHM systems and we showed that using proper LDPC codes a considerable improvement in the storage capacity is achievable. Figure 1 shows the storage capacity that is obtained by using LDPC codes and RS codes of different lengths and different decoding methods. For RS codes the maximum storage capacity is .5609 Gbits which is obtained when 2802 pages are stored and hard decision decoder was used. The maximum storage capacity that is obtained by using LDPC codes is .8423 Gbits that is obtained when 4600 pages are stored. We note that this capacity is about 50 percent higher than that of the RS codes. This sizable increase in the capacity by the LDPC code can be explained by use of Fig. 1. When the number of pages is small, there is not much difference between the RS codes and the LDPC codes. This is because the information theoretic capacity of hard decision and soft-decision decoding are close to each other for a high SNR (or equivalently, a small number of pages). Moreover, RS codes have a good performance for such SNRs. However, when the number of pages increases and therefore SNR decreases the difference between the capacity of hard decision and soft-decision decoding increases. More importantly, LDPC codes maintain near the Shannon limit of performance for the low SNR, while the performance of RS codes is far from the Shannon limit in the low SNR. For this reason, the optimum number of pages for LDPC codes is higher than that for RS codes. We also note that the performance of LDPC codes with hard-decision decoding is about 25 percent higher than the maximum capacity of the RS codes. It is important to note that the full advantage of LDPC codes is obtained if we choose the optimum number of holograms ($M=4600$). Let us now specifically give one of the codes that we found. For the rate 0.85 we divided the page into four different regions each with a different noise power. Consider the code for which we have

$$d_1=3, d_2=4, d_3=7, d_4=10, d_c=40$$

where d_i is the degree of variable nodes of the bits from region i , and d_c is the degree of check nodes. Note that the degree distribution is very simple. The relative SNRs in different regions are assumed as

$$\begin{aligned} \text{SNR}_2 - \text{SNR}_1 &= 1.61\text{dB}, \\ \text{SNR}_3 - \text{SNR}_1 &= 2.80\text{dB}, \\ \text{SNR}_4 - \text{SNR}_1 &= 3.74\text{dB}. \end{aligned} \quad (1)$$

Figure 2 shows the performance of this code when the block length is $n=10^4$ and $n=10^5$. It can be noticed from the figure that for $n=10^5$ at the BER of 10^{-9} the gap from the capacity is only 0.65 dB and for $n=10^4$ this gap is 1.04 dB.

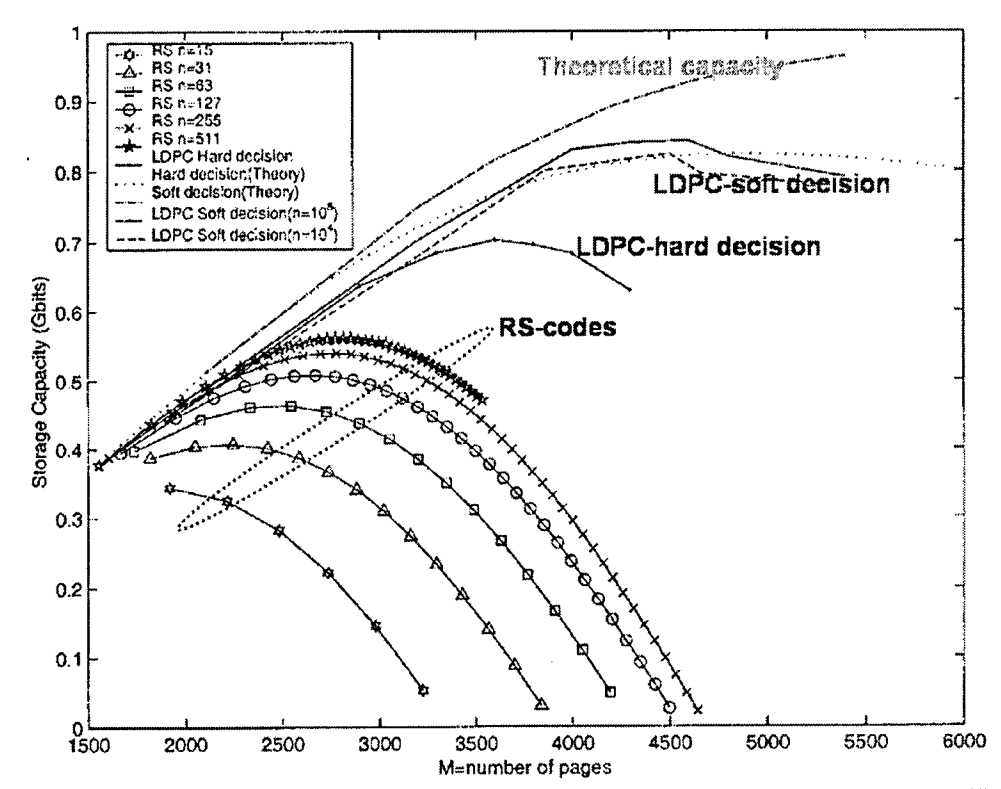


Figure 1 – Comparison between performance of LDPC codes of different lengths, different decoding (hard decision and soft decision) and Reed-solomon codes.

As we said earlier, the complexity of encoding of LDPC codes is not linear in block length. To speedup the encoding process we propose RA codes.

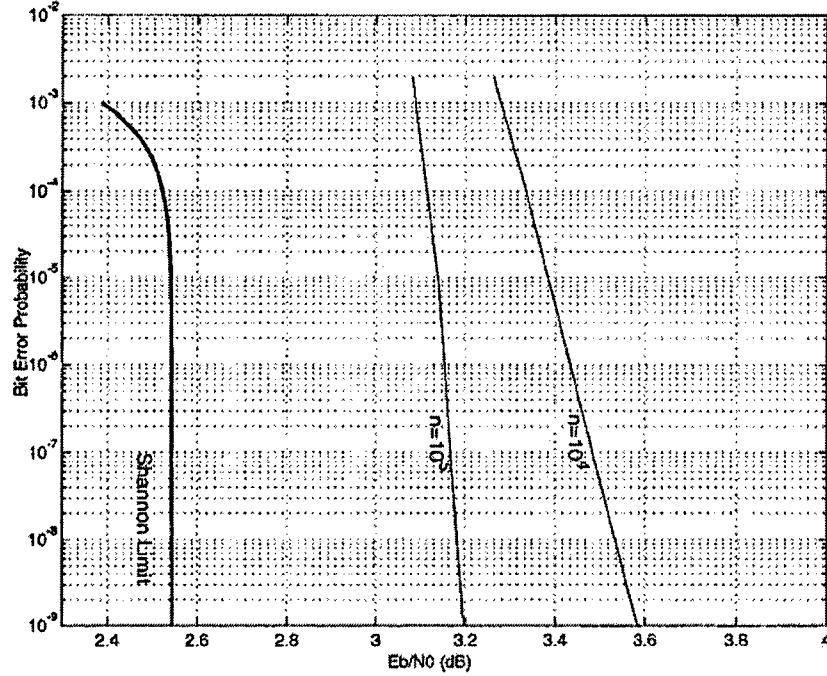


Figure 2 – Performance of the irregular LDPC code of rate 0.85.

3. Repeat-Accumulate (RA) codes for VHM Systems

The main drawback of LDPC codes is that they have a slow encoder. To overcome this problem we consider a special case of LDPC codes that is called Repeat-Accumulate codes. This code first is introduced in [9] for uniform channels. We designed and applied RA codes for non-uniform VHM systems. Figure 3 shows the Tanner graph of RA codes.

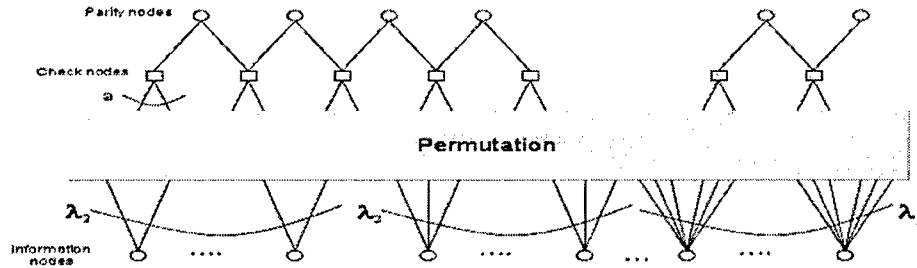


Figure 3 – Tanner Graph for RA codes.

As seen in Figure 3, there are two types of nodes, *variable nodes* (circles) and *check nodes* (squares). Variable nodes at the bottom are information nodes correspond to information bits and variable nodes at the top correspond to parity bits. The parameter λ_i is the fraction of edges between the information and the check nodes that are adjacent to an information node of degree i . Note that in a regular RA code we have $\lambda_i=1$; which

means all information bits have the same degree i . The parameter a in Figure 3 is the number of message bits that each time add to previous check bit to form current check bit as

$$p_0 = \sum_{j=1}^a m_{0,j}$$

$$p_i = p_{i-1} + \sum_{j=1}^a m_{i,j}$$
(2)

Here, p_i is the i^{th} parity bit and $m_{i,j}$ is a random message bit. Comparing the Tanner graph of RA codes with LDPC codes we note that the difference is that all parity bits in RA codes have degree two. Also the edges between check nodes and parity bits are connected in a systematic way (zigzag). This type of connection has two advantages. First it makes the encoding easy. Second we can reduce the error floor.

The parity check matrix of the RA codes is in the following form:

$$H = [H_1 | H_2]$$

in which H_2 is equal to

$$H_2 = \begin{pmatrix} 1 & 0 & 0 & 0 & 0 \\ 1 & 1 & 0 & 0 & 0 \\ 0 & 1 & 1 & 0 & 0 \\ \cdot & \cdot & \cdot & \cdot & \cdot \\ \cdot & \cdot & \cdot & \cdot & \cdot \\ \cdot & \cdot & \cdot & \cdot & \cdot \\ 0 & 0 & 0 & 1 & 0 \\ 0 & 0 & 0 & 1 & 1 \end{pmatrix}$$
(3)

The encoding system of this code is shown in Figure 4 where D represents a unit delay.

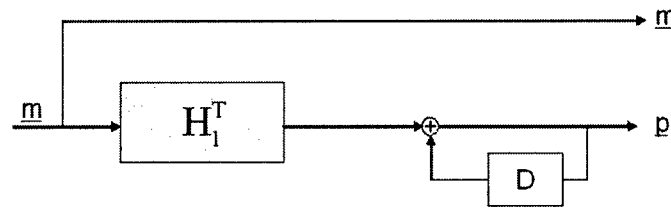


Figure 4 – Encoding block diagram for systematic RA codes

Two properties of the noise in the VHM systems are utilized in our scheme. One is that the noise level is small with respect to the signal level. For example, a raw BER of 10^{-3} to 10^{-6}

is typical. More importantly, the noise distribution is non-uniform and the bits at the center of the page can have much lower raw BER rates than those at the corners. It is worth noting that the matrix H_2 is associated with the parity bits. By choosing parity bits from the highly reliable pixels in the page (bits from the center of the page), we can decrease the error floor level significantly. This is because bits associated with H_2 will be less likely in error. Since we usually use high-rate codes in the VHM systems, the number of parity nodes is small compared to the code length. Thus, there exist enough bits to choose all the parity bits from the center of the page. Our experimental results show that the above method works very well in practice. In summary, the design of IRA codes for VHM systems is similar to the design of LDPC codes for these systems. However, the error floor problem needs more care. In LDPC codes it is usually enough to satisfy the condition for having a linear minimum distance. For IRA codes, the discussion in this section shows that although the minimum distance is usually small, using the non-uniformity of the raw BERs we can still reduce the error floor effect.

Figure 5 shows the performance of an IRA code that we designed for the same SNRs as (1), length 10^4 , and rate .9

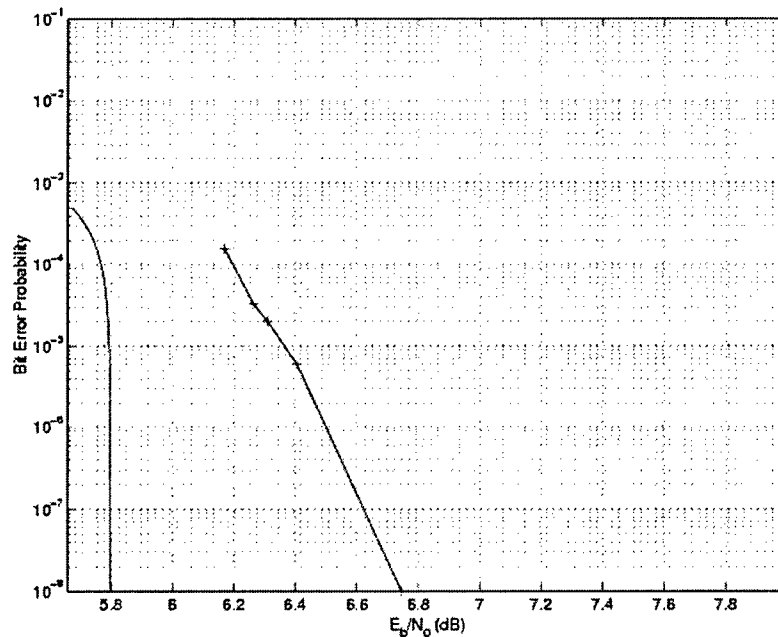


Figure 5 – Performance of the IRA code of length 10^4 and rate .9

Figure 6 shows the storage capacity that is obtained by using IRA, LDPC and Reed-Solomon (RS) codes. The LDPC codes and IRA codes have lengths $n=10^4$ and the RS codes have length 512. The LDPC codes and the RS codes are the same codes used before. The IRA and LDPC codes are decoded by the standard iterative decoding using soft information. Only hard decision decoding is considered for RS codes. We note that both LDPC and IRA codes result in a considerably higher maximum storage capacity (about fifty percent higher capacity) than the RS codes. Similar to LDPC codes the optimum number of pages for the IRA codes is higher than that of the RS codes.

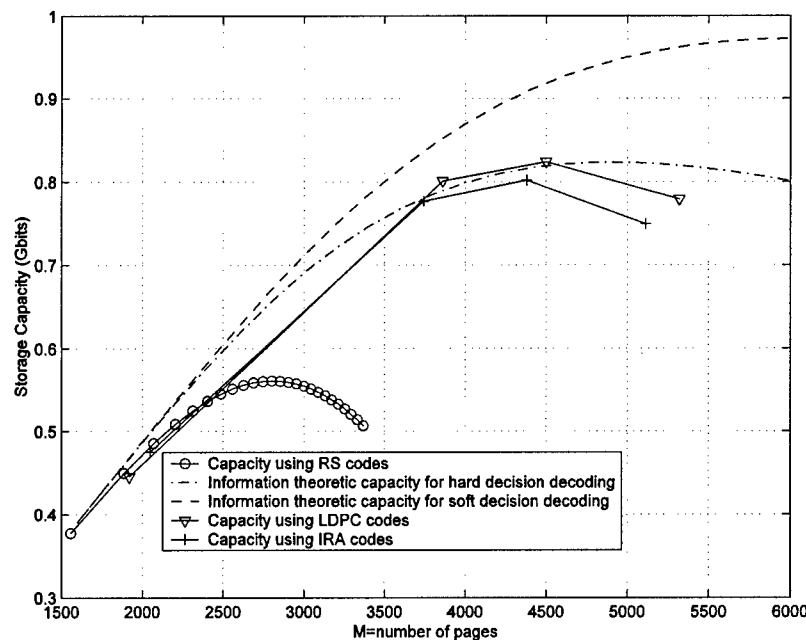


Figure 6 – Comparison of different coding schemes for a VHM system.

4. Other related works

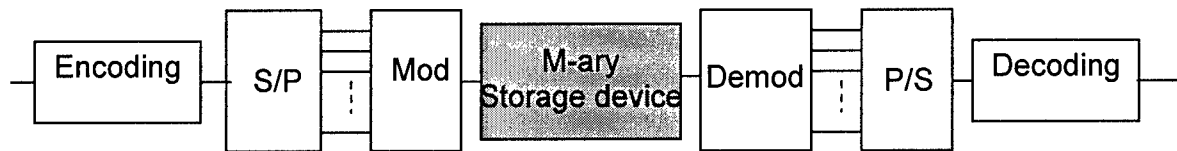
In the design of LDPC codes for holographic memories that are considered as non-uniform channels, we also came up with interesting design methodologies for some other related problems such as punctured LDPC codes [7] and unequal error protection LDPC codes [6]. In puncture codes we do not send some parity bits when the channel becomes better. This is equivalent to sending these bits through another channel having zero capacity. Therefore, we have a non-uniform channel as holographic memories. Additionally, in VHM systems,

different bits experiences different noise levels. Therefore, different levels of protection are needed that can be obtained by the unequal error protection codes.

We also developed an improved decoding algorithm for iterative decoding of LDPC codes [7],[8]. We showed that a gain of up to .5dB can be obtained by using the improved decoding algorithm in compare with the conventional message passing technique. We may use this algorithm for improving the performance of our codes in VHM system.

5. Future works

Combination of LDPC coding and M-ary storage. In this method we store more than one bit in each pixel. By M-ary storage, we can increase capacity and use the available SNR more efficiently. For future, we suggest using LDPC and IRA codes with higher level modulations like 8AM, 16AM, ...



6. References

- [1] H. Pishro-Nik, N. Rahnavard, J. Ha, F.Fekri, and A. Adibi, "Low-density Parity-check codes for volume holographic memory systems", *Applied Optics-IP*, Volume 42, Issue 5, pp 861-870, February 2003.
- [2] H. Pishro-Nik, N. Rahnavard, and F. Fekri, "Non-uniform error protection using low-Density parity-check codes", *Proceeding of the 40th Annual Allerton Conference on Communication, control, and computing*. Oct. 2002.
- [3]. H. Pishro-Nik, N. Rahnavard, F. Fekri, "Non-uniform Error Correction Using Low-Density Parity-check codes", submitted to *IEEE Transaction on Information Theory*, 2003.
- [4] H. Pishro-Nik, N. Rahnavard, F.Fekri, "Results on Non-uniform Error Correction Using Low-Density Parity-check codes", *IEEE Global Telecommunications Conference*, Dec. 2003.

- [5]. H. Pishro-Nik and F. Fekri, "Irregular Repeat Accumulate Codes for volume holographic memory systems ", Journal of Applied Optics, Vol. 43 No.27, September 2004
- [6] N. Rahnavard, H. Pishro-Nik, F. Fekri, " Unequal error protection using low-density parity check codes", in 2004 IEEE International symposium on Information Theory.
- [7]. Hossein Pishro-Nik, Faramarz Fekri, "Results on punctured low-density parity-check codes and improved iterative decoding techniques", submitted to IEEE Transaction on Information Theory, 2003.
- [8] Hossein Pishro-Nik, Faramarz Fekri," Improved Decoding Algorithms for Low-Density Parity-Check Codes", the 3rd international symposium on turbo codes & related topics, France, Sept. 2003.
- [9] H. Jin, A. Khandekar, and R. McEliece, " Irregular Repeat-Accumulate Codes ", 2nd international conference on turbo codes, September 2000.
- [10] M. Yang, Y. Li, and W. E. Ryan, " Design of Efficiently Encodable Moderate-Length High-Rate Irregular LDPC codes", Proceeding of the 40th Annual Allerton Conference on Communication, control, and Computing. Oct. 2002
- [11] M. Yang, and W. E. Ryan, " Lowering the Error-Rate Floors of Moderate-Length High-Rate Irregular LDPC codes", International symposium on Information Theory, 2003.

List of published or submitted papers resulting from this project:

1. H. Pishro-Nik, N. Rahnavard, J. Ha, F. Fekri, and A. Adibi, "Low-density Parity-check codes for volume holographic memory systems", Applied Optics-IP, Volume 42, Issue 5, pp 861-870, February 2003.
2. H. Pishro-Nik, N. Rahnavard, and F. Fekri, "Non-uniform error protection using low-density parity-check codes", Proceeding of the 40th Annual Allerton Conference on Communication, control, and Computing, , Urbana-Champaign, IL, CDROM, Oct. 2002.
- 3 . H. Pishro-Nik, N. Rahnavard, and F. Fekri, "Non-uniform Error Correction Using Low-Density Parity-check codes", accepted with minor revision in IEEE Transaction on Information Theory, accepted Dec. 2004.
4. H. Pishro-Nik, N. Rahnavard, and F. Fekri, "Results on Non-uniform Error Correction Using Low-Density Parity-check codes", in Proc. of GlobeCom. vol. 4, pp. 2041-2045, San Francisco, CA, Dec. 2003.

5. N. Rahnavard and F. Fekri, "Unequal error protection using low-density parity check codes", Proc. International Symposium on Information Theory, p. 449, Chicago, IL, June 2004.
6. N. Rahnavard, H. Pishro-Nik, and F. Fekri, "Unequal error protection using LDPC codes", submitted to IEEE Trans. On Communications, 2004.
7. Hossein Pishro-Nik, Faramarz Fekri, "Improved Decoding Algorithms for Low-Density Parity-Check Codes", Proc. 3rd international symposium on turbo codes & related topics, France, 2003.
9. H. Pishro-Nik and F. Fekri, "Irregular Repeat Accumulate Codes for volume holographic memory systems ", Journal of Applied Optics, Vol. 43 No.27, September 2004
10. H. Pishro-Nik and F. Fekri "Application of Irregular Repeat-Accumulate Codes to Holographic Storage Systems", Proc. 38th Annual Conference on Information Sciences and Systems, Princeton, NJ, March 2004, CDROM.
11. H. Pishro-Nik and F. Fekri "On Decoding of Low-Density Parity-Check Codes Over the Binary Erasure Channel", IEEE Transaction on Information Theory, vol. 50, no. 3, pp. 439-454, March 2004.

Part 4: Constrained Coding and Signal Processing for Holographic Data Storage

Shayan G. Srivinas, and Steven McLaughlin

Principal Investigator: Steven McLaughlin

Constrained Coding and Signal Processing for Holography

Abstract

The need for fast page-oriented data storage systems with ultra high memory and very fast data access has motivated research in optical holographic memories. In our initial proposal we described how we could increase data storage density in optical memories by using constrained coding. Increasing the bandwidth of the system by placing constraints on them can result in enhanced information storage per page for some choices of appropriate constraints. We highlighted the need for signal processing techniques to overcome noise and inter pixel cross talk due to imaging imperfections and optical effects. In this report, we will provide a summary of our coding and signal processing research during the three-year period. From a theoretical standpoint, the eventual goal is to develop a general information-theoretic framework that solves the open problem for exactly computing capacity and devising full rate and practically implementable codes for 2-D constrained channels. Further there are signal-processing challenges that accompany information processing in such devices.

1. Introduction

With ubiquitous computing and pervasive communication technologies, there is a need for devices that are ultra-fast and have very high storage densities. While current storage needs are being met, new storage technologies are being developed to keep in tune with the ever-increasing demand for information storage. Volume holographic memories (VHM) are potential solutions for optical storage. Storing gigabits of information throughout the *volume* of a medium, like a small LiNbO_3 crystal is very exciting albeit intriguing.

In holographic storage [11], an entire page of information is stored at once as an optical interference pattern within the photosensitive optical material by intersecting two coherent laser beams within the storage material. One of the beams carries the information while the other acts as a reference beam. Data can be perfectly recovered by illuminating the right reference beam to the interference pattern. Thus using volumetric approach, data can be stored and retrieved in pages in a parallel fashion. This method offers tremendous advantages in computational and storage requirements over conventional magnetic storage devices.

The fundamental limitations in the optical resolution [11] (ability of the crystal to resolve adjacent bits) of the photosensitive crystalline material envisages the need to construct modulation codes that mitigate these problems, and at the same time store more information bits. One such class of nonlinear binary codes is the Run Length Limited code (RLL code) [2].

RLL codes are common in digital storage systems to increase storage density, to ensure system timing, to combat inter-symbol interference (ISI), and for spectral shaping. By definition, a 2-D RLL code is a nonlinear mapping of a binary sequence to a sequence

that satisfies a (d_1, k_1, d_2, k_2) constraint, in which, two consecutive 1's are separated by at least d_1 0's, and at most k_1 0's along rows; and at least d_2 0's, and at most k_2 0's along columns. The capacity of the constraint channel is defined as

$$C_{2D} = \lim_{m,n \rightarrow \infty} \left(\frac{\log(N_{m,n}^{(d_1, k_1, d_2, k_2)})}{mn} \right), \text{ where } N_{m,n}^{(d_1, k_1, d_2, k_2)} \text{ denotes the number of valid}$$

2-D RLL sequences on a rectangular grid of dimensions $m \times n$.

The ideas relating to constrained systems dates back to the work by Jacques Hadamard and Leonard Euler who pioneered research on non-linear dynamical systems for applications in planetary motions and orbital paths. The study of constrained systems is an active area in the area of mathematics called symbolic dynamics. While one-dimensional constrained systems are well understood, there is very little known about the topological entropy and coding aspects for such systems in more than two dimensions. The general problem for computing capacity and designing rate efficient codes for 2-D RLL codes is an *open* problem [7] of significant interest to both theoreticians and engineers. Tight bounds [2] and efficient coding schemes [9] for 2-D RLL channels are known only in a few cases.

In this research report we highlight the ideas relating to capacity and coding schemes for a class of RLL constraints. The capacity bounds developed provide a quantitative insight to the amount of the information storage increase that can be theoretically possible. Further it is interesting to note that the coding schemes we developed are practical and can be easily implemented in a real time system.

The report is organized as follows. In the second section, we will briefly review the idea of optical information storage. In the third section, we will outline algorithms for estimating capacity of $(1, \infty, d, k)$ constraints. In the fourth section, we will highlight algorithms for constructing codes for $(d_1, \infty, d_2, \infty)$ constraints. In the fifth section, we will address some signal-processing issues related to misregistration effects and provide algorithms. Some of these techniques are applicable for general imaging systems. Finally we highlight some new research issues that we are currently investigating.

2. Overview of Optical Information Storage

Without any clever techniques, one information bit per pixel can be stored in an optical page of bits. Consider a scheme in which each pixel is divided into a $d_1 + 1 \times d_2 + 1$ grid. The elements inside the grid are binary constrained sequences such that a '1' represents the center of the pixel with '0's in a particular order. Thus we can imagine such super pixels with varying lengths and widths. This can be described as pulse width modulation in two dimensions. The schematic is illustrated in Figure 1. The constrained channels have a capacity given by C_{2D} which was defined earlier. Hence the theoretical storage density (D) is given by $D = (d_1 + 1)(d_2 + 1)C_{2D}$. Depending on the quantity C_{2D} we can determine the effective storage density that is possible by using constrained codes. There are instances when certain constraints yield zero capacity, which implies that there is no storage density achievable. However $C_{2D} > 0$ it is possible to store more than one bit per

pixel. An important step to understanding how this works is to think of this coding scheme as a way in which we try to store more bits than usual by sub dividing a pixel into a more fine grid array and enforce constraints on them. To give a physical meaning to the information conveyed in this block, 1's represent the center of the pixel and 0's ensure that interpixel cross talk is kept at premium. Thus we can think of information being smeared across multiple pixels and the goal is to recover the encoded bits losslessly. As mentioned before, analytically computing C_{2D} is extremely difficult and is an active area of research in information theory.

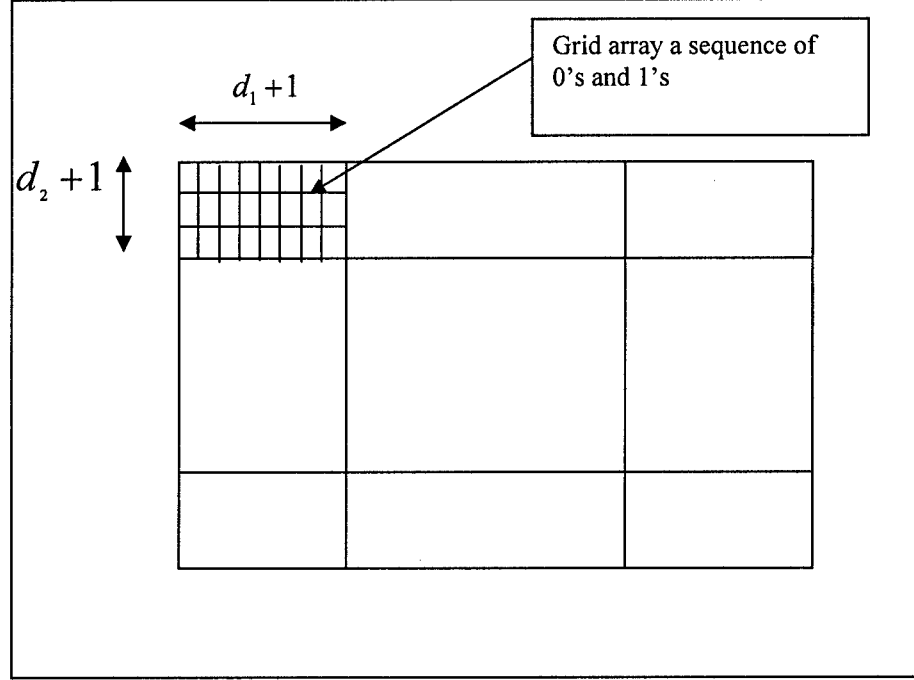


Figure 1. Schematic of a 2-D RLL Code on a Rectangular Plane

3. Runlength-Limited Constrained Coding

With the basic idea as to how we can store more bits than usual, we will consider developing algorithms for constructing valid constrained arrays, for estimating capacity and deducing coding schemes with rates close to the derived bounds. In the following sub sections we will consider a family of constrained parameters.

3.1 Algorithms for constructing $(1, \infty, d_2, k_2)$ constrained arrays and capacity Bounds [4]

A: Adjacency Approach

The capacity problem is combinatorial in nature. As a precursor to estimating capacity, we consider algorithms for constructing valid arrays satisfying

$(1, \infty, d_2, k_2)$ constraints on a $m \times n$ grid. These constructions provide an insight to the structure of the coded arrays and a means towards getting to capacity. The basic idea behind constructing arrays satisfying $(1, \infty, d_2, k_2)$ constrained arrays is to recognize that the row constraint is just a first order Markov process on the valid blocks of column vectors under the merger operation that is commutative. The idea is to explore the well-known adjacency approach applicable in a vector setting.

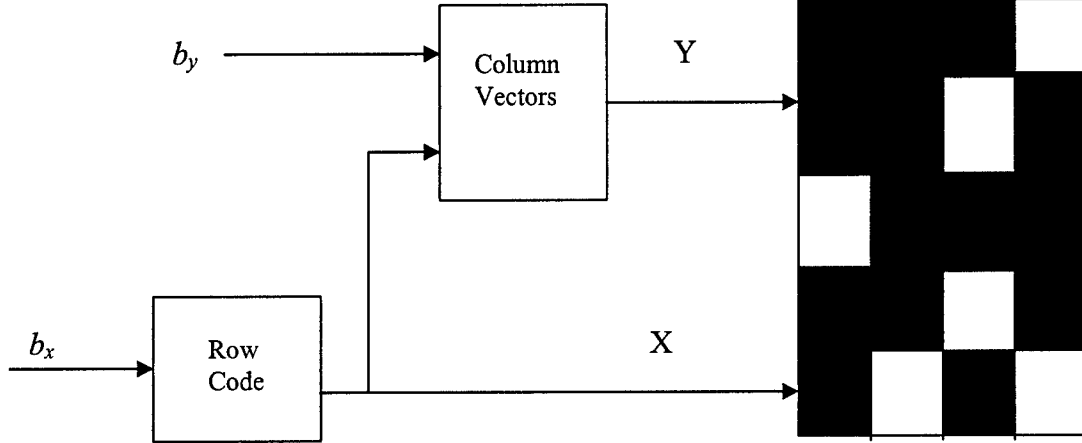


Figure 2: Schematic of the encoder for $(1, \infty, 1, \infty)$ code on a 5x4 Grid.

The model shown in Figure 2 comprises of two encoders. The first encoder takes binary input b_x and produces a $(1, \infty)$ constrained sequence along the bottom row. The second encoder takes binary input b_y and produces a set of (d, k) constrained column vectors according to a second constrained graph. The states of the second constrained graph are the (d, k) constrained column vectors. These states are driven by an adjacency matrix $A = [a_{ij}]$ such that for any two vectors v_i and v_j , $a_{ij} = 1$, if $v_i \bullet v_j = 0$ (dot product on the real field). The encoding is done as follows. First, for every set of zeros that occur in the bottom row, we place column vectors from the second encoder. For the remaining positions (positions of 1's that occur in the bottom row), a column vector that is orthogonal to both its previous and next vector is placed. The following example illustrates the procedure.

Example: Figure 2 shows the placement of sequences on a 5x4 grid. The black squares in Figure 2 denote a zero while the white ones denote a one. The phrases “01” appear twice along the bottom row. Column vectors $(0010)^T$, $(0000)^T$, $(0101)^T$ and $(1000)^T$ are stacked above the bottom row. It is to be noted that vectors $(0000)^T$ is orthogonal to $(0010)^T$ and $(0101)^T$ while $(1000)^T$ and $(0101)^T$ are orthogonal. The column vectors can be represented by a finite state Markov chain that can take the following set of orthogonal vectors v_i in 4 dimensions namely, $(0000)^T$, $(0001)^T$, $(0010)^T$, $(0100)^T$, $(1000)^T$, $(1010)^T$, $(0101)^T$ and $(1001)^T$. The graph G is described by the adjacency matrix $A = [a_{ij}]$ where $a_{ij} = 1$, if $v_i \bullet v_j = 0$, the dot product defined on the real field. The adjacency matrix A is given by,

$$A = \begin{bmatrix} 1 & 1 & 1 & 1 & 1 & 1 & 1 & 1 \\ 1 & 0 & 1 & 1 & 1 & 1 & 0 & 0 \\ 1 & 1 & 0 & 1 & 1 & 0 & 1 & 1 \\ 1 & 1 & 1 & 0 & 1 & 1 & 0 & 1 \\ 1 & 1 & 1 & 1 & 0 & 0 & 0 & 0 \\ 1 & 1 & 0 & 1 & 0 & 0 & 0 & 0 \\ 1 & 0 & 1 & 0 & 0 & 0 & 0 & 0 \\ 1 & 0 & 1 & 1 & 0 & 0 & 0 & 0 \end{bmatrix}$$

The matrix A is symmetric and has a neat structure. This property is due to the $(1, \infty)$ row code. It is essential to note that the adjacency matrix scheme for constructing codes is feasible as long as the column height is small and finite. Applying this scheme for constructing codes on an infinite grid is practically impossible due to exponential increase in the number of states of the state machine that describes the adjacency matrix. At this point, the reader might wonder if the scheme has any advantage compared to just letting a set of column vectors of length N driven by a constrained graph without the row encoder. It is possible to have $S_N - S_{N-1}$ savings in the number of states while maintaining high efficiency with the proposed scheme ($S_N \equiv$ Number of states for vectors of length N).

The following theorem provides the capacity bounds for $(1, \infty, d_2, k_2)$ constraints. Here λ_m denotes the eigen-value of the adjacency matrix for column vectors of length m .

Theorem 1: The capacity of $(1, \infty, d_2, k_2)$ constraints is bounded as

$$\sqrt[p]{\frac{\lambda_{p+2q}}{\lambda_{2q}}} \leq C \leq \frac{1}{m} \lambda_m$$

The lower bound follows from maximizing the Raleigh quotient of the eigen-value relation for the adjacency matrix and noting that adjacency matrix is symmetric using the exact same approach taken by Calkin and Wilf [2]. The upper bound follows from the fact that $\left\{ \frac{1}{m} \lambda_m \right\}_{m=1}^{\infty}$ is a decreasing sequence in m .

The fact that computing eigen-values can be cumbersome for large values of m makes the adjacency approach less attractive. Further deducing coding schemes is fairly complicated.

To circumvent the complexity of storage issues we propose an alternative approach called the iterative approach whose details are outlined in the next subsection. The iterative approach has very low time and space complexities for writing valid sequences on a 2-D grid.

B: Iterative Approach

In this section we highlight a strategy for encoding $(1, \infty, d, k)$ sequences on an infinite plane. The key ideas behind the approach are as follows:

- An infinite sequence of phrases is constructed along the first column by a random walk on a 1-D (d, k) constrained graph.
- For every '1' that occurs along the first column, a '0' is placed adjacent to it. This bit stuffing ensures that the row constraint is satisfied.
- (d, k) sequences are constructed in the second column consistent to the previous step. The underlying process is non-stationary as zero padding is done to satisfy the d constraint and the state machine is triggered at an appropriate pre-determined state to satisfy the k constraint.

Unlike the previous method, the iterative approach is not restricted by space complexity and does not require encoding in blocks.

Outline of Algorithm

There are totally $k + 1$ states in the state machine.

1. Introduce the following definitions:

c = Column Number

f = Look ahead free position where a bit can be written (anticipation)

p = Position where a '1' was most recently written (memory)

a = Look ahead occupied position of a '0' (anticipation)

2. Along the first column, make an infinite random walk on a constrained graph (G).

Initialize: $c = 2$

3. Start from the column ' c '.

Initialize $f = 1$ and $p = f$;

➤ Locate a .

➤ Starting from state S_1 , make a random walk of length $a - f$ on graph G. Denote this sequence as Y.

4. Update p , f and a .

5. If $f - p < d$

➤ Stuff $d - f + p$ zeros to satisfy 'd' constraint. Update f .

➤ Make a random walk of length $a - f$ from state S_d . Let this sequence be Y.

Else

➤ Make a random walk of length $a - f$ from state S_{f-p} .

End

6. Loop over Step 4 till all rows are filled.

7. For every '1' that occurs in the current column, stuff a '0' adjacent to it.

8. $c \leftarrow c + 1$

- 9. Loop over Step 3 till all columns are filled.
- 10. Stop

Theorem 2: The iterative algorithm enumerates all valid constrained arrays satisfying $(1, \infty, d, k)$ constraints on a $m \times n$ grid.

An open issue at this point is to determine the capacity using the iterative algorithm as we believe that this will solve the capacity problem.

4. Algorithms for Constructing $(d_1, \infty, d_2, \infty)$ Constrained Arrays: Capacity Bounds and Coding Schemes [3]

In this section we consider a second family of constrained sequences namely $(d_1, \infty, d_2, \infty)$ RLL constraints. The key questions again are, how do we algorithmically enumerate all sequences satisfying $(d_1, \infty, d_2, \infty)$ RLL constraints on a $m \times n$ grid? What are the fundamental limits [1] for the maximum information rate of noiseless $(d_1, \infty, d_2, \infty)$ constrained channels? How do we construct codes for mapping raw bits to valid 2-D coded arrays?

We develop two enumeration techniques for constructing $(d_1, \infty, d_2, \infty)$ arrays.

- Approach #1: The basic idea is to generate an exhaustive set of column vectors of length m , satisfying the 1-D (d_2, ∞) constraint. The vectors are then horizontally concatenated side-by-side in such a way that every column vector is orthogonal to all the previous d_1 column vectors.
- Approach #2: In this approach, an infinite sequence of column vectors satisfying (d_2, ∞) constraint is constructed along the first column. As a first step, for every '1' that occurs in the first column, d_1 zeros are stuffed adjacent to it so that (d_1, ∞) row constraint is satisfied. In the second step, (d_2, ∞) sequences are constructed in the next columns conditioned to the already stuffed 0's. The two steps are repeated for infinitely many columns.

4.1 Tiling Algorithms

A: Tiling Scheme – A

The basic idea behind tiling scheme-A is to first obtain a set of all (d_2, ∞) column vectors of length m and then merge these vectors according to certain conditions such that the resulting array satisfies the overall constraints. Before beginning with the outline of the algorithm, we will present a few facts for sequentially writing vector sequences to obtain a valid array.

Let Q denote the set of all (d_2, ∞) column vectors of length m . It is straightforward to note that the column wise concatenation of a sequence of vectors $z_i^{(m)} \in Q$, and $i = 1, \dots, n$ resulting in a block that satisfies the constraints has a memory

d_1 . The following lemma provides the necessary and sufficient conditions that the column vectors must satisfy for a valid 2-D array.

Lemma 1: Let $z_i^{(m)}$ and $z_j^{(m)} \in Q$ denote column vectors on a $m \times n$ grid satisfying the constraints. The vectors $z_i^{(m)}$ and $z_j^{(m)}$ ($i < j$) satisfy the set of orthogonal conditions given by,

$$z_i^{(m)} \cdot z_j^{(m)} = 0, 1 \leq i \leq n \text{ and } i+1 \leq j \leq i+d_1.$$

From Lemma 1, we obtain a tiling algorithm summarized below.

Outline of Algorithm-A

1. Initialize: $j = 2$. Choose any random vector $z_1^{(m)} \in Q$ for the first column.
2. Start from column j . Choose a vector $z_j^{(m)} \in Q : z_j^{(m)} \cdot z_i^{(m)} = 0$ for i in the range $\max\{1, j-d_1\} \leq i \leq j-1$.
3. $j \leftarrow j+1$. Go to the next column.
4. Iterate over Step 2 for all the n columns.

It is to be noted that the time complexity of the Algorithm-A is proportional to the number of the columns sequentially written and computations involve calculating the conditions specified in Lemma 1. However the space complexity of the Algorithm-A is exponential in m .

B: Tiling Scheme-B

Consider a (d_2, ∞) constrained graph shown in Figure 3. Denote the states sequentially as $\alpha_0, \alpha_1 \dots \alpha_{d_2}$. The key ideas behind the algorithm are summarized as follows:

- A sequence of phrases (a phrase is an all zero sequence followed by a '1') is constructed along the first column by a random walk on a (d_2, ∞) constrained graph G shown in Figure 3.
 - For every '1' that occurs in the first column, d_1 zeros are stuffed adjacent to it (i.e., to its right). This 'bit-stuffing' ensures that the horizontal constraint is satisfied.
- (d_2, ∞) constrained sequences are constructed in the next column consistent with the 'bit-stuffing' in the previous step, by a random walk on G . Steps 2 and 3 are iterated for subsequent columns.

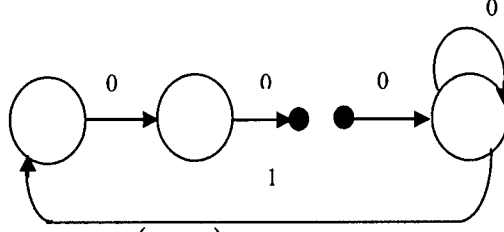


Figure 3: (d_2, ∞) Constrained Graph G .

We summarize the ideas in an algorithm below.

Outline of Algorithm-B

1. Initialize: $j = 1$.
2. Start from column j ; along the vacant spaces in column j , make a random walk on a (d_2, ∞) constrained graph G starting from state α_{d_2} .
3. For every '1' that occurs in column j , stuff d_1 zeros adjacent to its right.
4. $j \leftarrow j + 1$. Go to the next column.
5. Iterate from Step 2 for all the n columns.

It is clear that the vacant spaces along the first column will be the entire column length m but for subsequent columns, the vacant spaces are dictated by zero bit stuffing induced by the previous d_1 columns. It is easy to observe that the random walk process in Algorithm-B is shift invariant. Further this is not a maxentropic random walk on G due to zero bit stuffing. We note that the algorithm does not require writing sequences in blocks of column vectors and circumvents the storage overheads in Algorithm-A. We conclude this section by noting the fact that both the tiling schemes are equivalent. The result is stated in Theorem 3. The proof can be straightforwardly obtained by induction on the number of columns.

Theorem 3: Algorithm-A and B are equivalent and have the same maxentropic rate.

4.2 Capacity Bounds

The tiling schemes presented in Section 4.1 provide a construction for enumerating all valid 2-D sequences on a rectangular grid. The structure of the tiling algorithms will be useful for deriving bounds for capacity and for constructing codes. In this subsection we will derive capacity bounds.

In Theorem 4, we obtain a lower bound for the capacity of the constraints using combinatorial analysis. The lower bound is derived using the fact that the set of all valid sequences written along the vacant spaces of the columns is greater or equal to the set of all valid (d_2, ∞) column vectors that can be written in the same space.

Theorem 4: The capacity of the constraints is lower bounded as,

$$C \geq \lim_{m \rightarrow \infty} \frac{1}{m} \left[\frac{m+d_2}{d_2+1} \right] \left[\frac{m-w_1+d_2}{d_2+1} \right] \dots \left[\frac{m - \sum_{j=1}^{d_1-1} w_j + d_2}{d_2+1} \right] \sum_{w_{d_1}=0} P_{w_1 w_2 \dots w_{d_1}} \log(|S^{(d_1+1)}|)$$

$$|S^{(d_1+1)}| = \sum_{w_{d_1+1}=0} \left[\frac{m - \sum_{j=1}^{d_1} w_j + d_2}{d_2+1} \right] T_{w_{d_1+1}}(x), x = m - \sum_{j=1}^{d_1+1} w_j - (w_{d_1+1} - 1)d_2$$

where, $P_{w_1 w_2 \dots w_{d_1}}$ is the joint pmf of the set of all (d_2, ∞) column vectors with Hamming weights w_1, w_2, \dots, w_{d_1} respectively in the first d_1 columns; $|S^{(d_1+1)}|$ is the total number of all valid (d_2, ∞) column vectors in column $d_1 + 1$.

The joint probability mass function in Theorem 4 can be obtained as

$$P_{w_1 w_2 \dots w_{d_1}} = \prod_{j=1}^{d_1} P(W_j = w_j | W_{j-1} = w_{j-1}, \dots, W_1 = w_1) \quad (1)$$

The conditional pmf in (3) can be obtained as,

$$P(W_j | W_{j-1}, \dots, W_1) = \frac{T_{w_j} \left(m - \sum_{k=1}^j w_k - (w_j - 1)d_2 \right)}{|S^{(j)}|} \quad (2)$$

It is interesting to note that the lower bound can be numerically computed. In Theorem 5 we obtain an upper bound for the capacity of the constraints. Let $Z_i^{(m)}$ denote the random variable representing the i^{th} column vector in a valid 2-D array. Clearly the index i is also the time index since we are sequentially writing the column vectors. The following proposition can be directly inferred from Algorithm-A.

Theorem 5: The combinatorial bound in Theorem 4 is exactly equivalent to writing the alphabets 0 and 0^{d_2} in an i.i.d fashion along the void spaces of the columns created by the horizontal bit stuffing and is given by,

$$R \geq \sup_{0 \leq p \leq 1} \frac{h(p)}{(1 + d_1 p)(1 + d_2 p)}$$

Proposition 1: The conditional pmf $P_i(Z_i^{(m)} | Z_{i-1}^{(m)} \dots Z_1^{(m)}) = P_i(Z_i^{(m)} | Z_{i-1}^{(m)} \dots Z_{i-d_1}^{(m)})$ and is independent of i .

Using Proposition 1, we derive an upper bound for the capacity of the constraints.

Theorem 6: The capacity of the constraints is upper bounded by,

$$C \leq \frac{1}{m} H(Z_{d_1+1}^{(m)} | Z_{d_1}^{(m)}, \dots, Z_1^{(m)}),$$

where

$$H(Z_{d_1+1}^{(m)} | Z_{d_1}^{(m)}, \dots, Z_1^{(m)})$$

denotes the conditional entropy rate of the first d_1 columns.

The joint pmf in Theorem 5 can be obtained using the chain rule and Markovity of tiling scheme-A. It can be again noted that the bound in Theorem 5 can be numerically computed. We will now deduce a simple corollary from Theorem 5.

Corollary 1: Capacity is bounded by

$$\frac{m}{m+d_2} R_A^{(m)} \leq C \leq R_A^{(m)}, \text{ where, } R_A^{(m)} = \frac{1}{m} H(Z_{d_1+1}^{(m)} | Z_{d_1}^{(m)}, \dots, Z_1^{(m)})$$

It can be noted that Theorems 4, 5 and 6 can be used to obtain numerical estimates for capacity. It is interesting to note that the bounds are based on the stationary assumption in the underlying random process. However noting that the 2-D RLL process is non-stationary can further tighten these bounds. In other words non (d_2, ∞) sequences but satisfying the overall column constraints can be placed along the void spaces of the columns. The investigation of these aspects is part of the journal paper and omitted here for brevity.

4.3 Coding Schemes

In this subsection we will discuss a coding scheme based on the well-known state splitting algorithm [9] and the tiling algorithm-B for mapping raw bits to valid 2-D coded arrays.

Constructing the Encoder

The following steps illustrate the encoding procedure.

1. Choose integers p and q (relatively prime) such that $\frac{p}{q} \leq C$, where C is the lower bound for the capacity. Obtain the q^{th} power of the (d_2, ∞) constrained graph, perform the basic v-consistent splitting [7] and obtain the final encoder graph G' based on the state splitting algorithm.
2. Initialize column $i=1$.
3. Map the raw binary sequences to coded sequences along the vacant spaces of column i

4. For every '1' occurring in column i of the coded array, stuff d_1 zeros to the right along the next d_1 consecutive columns.
5. Go to the next column and iterate from Step 3 for the remaining columns.

After steps 1 through 5, we finally obtain the 2-D coded array.

Decoding Process

The decoding process is simple and follows the encoding principle. Initialize $i = n$, i.e., the last column of the coded array.

1. Look back from columns $i - d_1$ through $i - 1$ and identify all the ones occurring in these columns.
2. Remove the stuffed zeros occurring to the right of these ones along the next d_1 columns.
3. The resulting sequence is the code from the encoder graph G' .
4. Go to the previous column and iterate from Step 1 to obtain all the coded bits.
5. Decode the original p bits from the coded binary q blocks.

We will illustrate the encoding process for $(3, \infty, 3, \infty)$ RLL constraints. We obtained an upper bound as 0.3530 for these constraints. Also the bit stuffing lower bound [12] is 0.3402. Thus we can justify a rate 1/3 code.

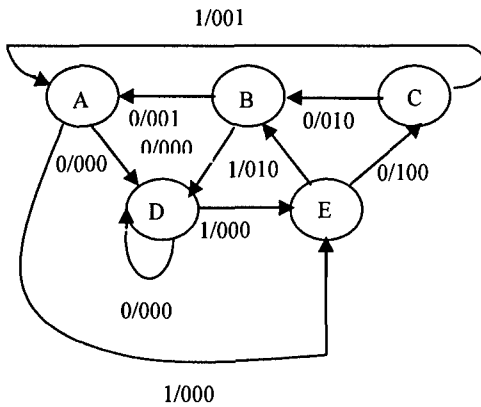


Figure 4: Encoder Finite State Transition Diagram (G')

0	0	0	1	0
0	0	0	0	0
0	0	0	0	1
1	0	0	0	0
0	1	0	0	0

Stuffed zeros

Figure 5: Coded Array on a 5x5 Grid

From step 1 of the encoding process, we obtain the final encoder graph shown in Figure 4. Suppose we have an input sequence 101100, with the starting state 'A', we obtain a 2-D coded array on a 5x5 grid as shown in Figure 5.

4.4 Numerical Results

In this section we evaluate numerical bounds for some cases of d_1 and d_2 . In Table 1, we compare the lower and upper bounds obtained from Theorems 4 and 6 with the bit-

stuffing lower bounds in [6] and the analytical formula for the upper bound in [8] (Theorem 8) for a class of symmetric (d, ∞, d, ∞) constraints. It is interesting to note that our upper bound is in close agreement to the bit-stuffing lower bound in around 2%. The upper bound was evaluated for a column length $m=12$. We conjecture that the upper bounds achieve a steady state for columns lengths with Hamming weights around 5. The lower bound was evaluated for $m=165$ using the analytical result in Theorem 3. Table 2 shows the capacity estimates for some cases of $(2, \infty, d, \infty)$ constraints. It is worth noting that our codes are practical, fixed length in nature and can be easily implemented in a real time system.

d	Upper Bound	Kato's Upper Bound	Lower Bound	Bit-stuffing Lower Bound
1	0.5932	1.000	0.5031	0.5878
2	0.4294	0.7501	0.3590	0.4267
3	0.3530	0.6206	0.2859	0.3402
4	0.3078	0.5366	0.2414	0.2858

Table 1: Capacity Estimates for (d, ∞, d, ∞) Constraints.

d	Upper Bound	Lower Bound
3	0.3805	0.3370
4	0.3761	0.3139
5	0.3508	0.2929

Table 2: Capacity Estimates for $(2, \infty, d, \infty)$ Constraints.

Thus from the theorems in section 4.2 and the coding scheme in section 4.3, we can obtain the following storage densities on an optical disk. **It is indeed very interesting to note that we get almost 6X-increased storage using our algorithms reported in this report.**

d	Lower Bound	Storage Density
1	0.5031	2.0124
2	0.3590	3.2310
3	0.2859	4.5744
4	0.2414	6.035

Table 3: Achievable storage densities using our algorithms for (d, ∞, d, ∞) Constraints.

5. Signal Processing for misregistration [10]

The invention of new data storage techniques requires the design of sophisticated signal processing algorithms to combat 2-D inter symbol interference, for noise removal and to handle misregistration in these systems. Some of the algorithms that we have developed here are applicable to general imaging systems not necessarily specific to volume holographic systems.

The detection and imaging process in most systems [11] is not always guaranteed perfect. The input spatial light modulator (SLM) is not always accurately imaged to the array of detector pixels. Any lateral offset (misalignment), optical distortion and scaling error can introduce interpixel cross talk and introduce artifacts in the received signal before any signal reconstruction procedure can be carried out. In this section we primarily focus on pixel misregistration problem. We consider the problem for handling rotationally misaligned systems. Rotational misalignments lead to fractional shifts that are not constant over pixels. In other words, pixels that are farther away from the center suffer more severe distortion than those at the center. Our work in this paper is motivated to extend the idea of handling fractional shifts for rotational distortion. Our algorithm is in general applicable for rotationally misaligned systems with square apertures and for holographic systems with low fill factors in the transmitter and detector arrays.

Figure 6 shows the schematic of spatially displaced images of SLM pixels relative to Charged Coupled Device (CCD) pixels.

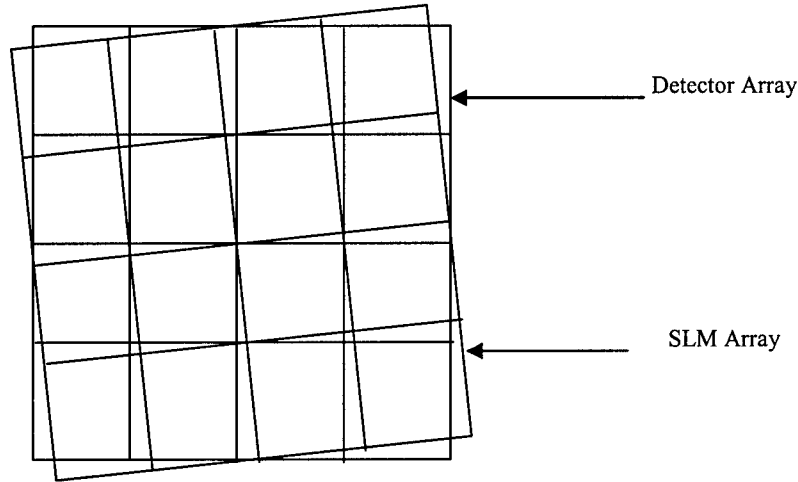


Figure 6: Rotational Misalignment of the SLM array with respect to the detector

The following theorem provides an upper bound on the number of bits that can be likely recovered with rotational misalignment.

Theorem 8: For $2m \times 2m$ equally likely binary bits of transmitted signal, at most $4m^2(1 - T_{loss})$ bits can be recovered from rotational misalignment. The parameter T_{loss} is given by,

$$\begin{aligned}
T_{loss} &= \frac{1}{2} pq \\
p &= 1 + \cot \alpha - \sin \alpha - \cot \alpha \sin \alpha \\
q &= 1 - \cos \alpha + \tan \alpha - \sin \alpha \tan \alpha
\end{aligned} \tag{3}$$

We note that the loss function T_{loss} is periodic with $\pi/2$ and the maximum loss is around 0.18 bits per pixel and occurs at angle $\alpha = \pm n\pi/4$. Figure 7 shows a plot of the loss function for $0 \leq \alpha \leq \pi/2$.

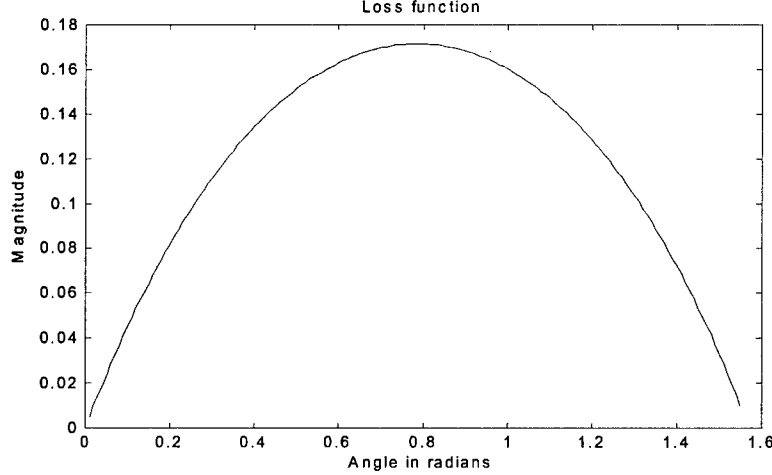


Figure 7: Loss as a function of the angle of rotation

However in the presence of noise, the transmitted pixels can suffer errors. In such cases we can model the channel as a binary symmetric channel with capacity C_{BSC} . The number of bits that can be recovered losslessly is now at most $4m^2(1-T_{loss})C_{BSC}$. It must be noted that the number of transmitted bits lost due to misalignment is not significant for small angles. However the inter-pixel interference with additive noise makes the problem difficult for signal recovery.

5.1 Channel Model and Problem Formulation

The spatial sampling rate is determined by the spacing of the pixels in the SLM and we assume this to be identical to the aperture width D . The pixel-spread function is the convolution of the space-invariant impulse response (due to the aperture) with the original pixel shape. The space-invariant impulse response is determined by the continuous space Fourier transform of the aperture shape. With a square aperture, the impulse response is a 2-D separable sinc function in the x-y plane given by,

$$h(x, y) = c^2 \int_{-0.5g_{SLM}}^{0.5g_{SLM}} \sin c(x-x') dx' \int_{-0.5g_{SLM}}^{0.5g_{SLM}} \sin c(y-y') dy' \tag{4}$$

where, g_{SLM} is the SLM fill factor where most of the intensity is captured, the variables x, x', y and y' are in the units of the pixel dimensions and the normalizing constant c is chosen so that $\int_{-\infty}^{\infty} \int_{-\infty}^{\infty} h^2(x, y) dx dy = 1$.

We note that the $h(x,y)=1$ when evaluated at the center of the SLM pixel and is oscillatory decaying along both the axes.

The angle of rotation α is positive in the clockwise direction. The coordinates of the SLM with respect to the detector can be obtained by the rotational transform R given by,

$$R = \begin{pmatrix} \cos \alpha & -\sin \alpha \\ \sin \alpha & \cos \alpha \end{pmatrix} \quad (5)$$

The received signal at the detector pixel $d(m,n)$ is given by,

$$d(m,n) = \int_{-0.5g_{CCD}}^{0.5g_{CCD}} \int_{-0.5g_{CCD}}^{0.5g_{CCD}} \left(\sum_{m_i, n_i} g_{m_i, n_i}(x,y) \sqrt{t(m_i, n_i)} \right)^2 dx dy \quad (6)$$

where, g_{CCD} is the CCD fill factor where the most of the intensity at the detector pixel is captured. The term $t(m_i, n_i)$ denotes the binary signal from the SLM pixel with discrete index (m_i, n_i) that overlaps with the detector pixel with discrete index (m, n) . We note that for small angles α , the indices (m_i, n_i) of the SLM pixels contributing to the cross talk terms in the detected signal $d(m,n)$ are due to $(\lceil m \cos \alpha + n \sin \alpha \rceil, \lceil -m \sin \alpha + n \cos \alpha \rceil)$ and its three neighbors on the left, bottom and left-diagonal. Referring to Figure 1, let us fix the origin as the center of the grid array. The signal at the detector pixel with right top corner coordinates (1,2) is indexed as $d(1,2)$ and has energy mainly contributed by the SLM pixels $t(2,2), t(2,1), t(1,2)$ and $t(1,1)$.

The kernel $g_{m_i, n_i}(x,y)$ in (6) is the rotated version of the function $h(x,y)$ and is given by,

$$g_{m_i, n_i}(x,y) = \frac{1}{|R|} h(x-a)h(y-b) \quad (7)$$

where, $(a,b) = (m_i - 0.5, n_i - 0.5)R^T$. Also $|R|=1$ since R is orthonormal.

Figure 8 shows the sketch of the kernel $g(x,y)$ centered at the point (0.5,0.5). We can imagine a tiling of such kernels at the center of each SLM pixel. These kernels low pass filter the transmitted signal causing pixel blur. The effect of rotation causes non-uniform inter-pixel interference at the intended detector pixel.

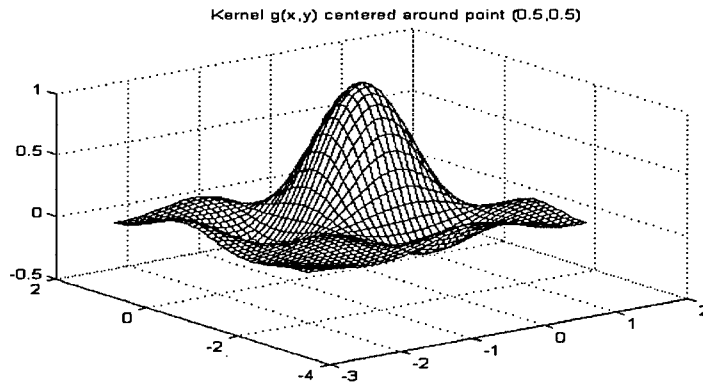


Figure 8: Schematic of the rotated two-dimensional kernel $g(x,y)$

The goal of the problem is to recover the transmitted bits from the detected signal $d(m,n)$.

5.2 Algorithm for Signal Recovery

We consider small angles of rotational misalignment i.e., less than around 3 degrees from a practical perspective. Large angles of rotation can always be compensated by carefully aligning the parts till the point where it is difficult to fine-tune the angle alignment. Without loss of generality, we assume the detector array to be a square grid of size $2m \times 2m$. We define a coordinate system of the detector array as follows. The coordinate of the center of the grid array is designated as the origin $(0,0)$. The index for a detector pixel is identified by the coordinate of its right top corner.

From the structure of equation (6) we observe that the system is fundamentally non linear and anti causal. The non-linearity is due to the cross terms in the squaring process. The non-causality arises because we cannot initiate a recursion without the knowledge of a few transmitted bits.

In order to facilitate a recursion, we need to initialize the SLM pixels in the boundary layers to zero. To determine the number of such layers that are initialized to zero, we compute the coordinates of the SLM array that just exceeds the range of the detector array. Consider the column of pixels at the right most ends. The coordinate of their right top corner $(m, y)^T$ after rotational transform is obtained as $(m \cos \alpha - y \sin \alpha, -m \sin \alpha + y \cos \alpha)^T$. The point where is the ordinate y exceeds m is given by,

$$-m \sin \alpha + y \cos \alpha > m \quad (8)$$

From (8) we infer that we need to set the top $\lfloor m(1 - \sin \alpha) / \cos \alpha \rfloor$ layer of SLM pixels to zero. Similarly by symmetry we set the bottom, left and right most $\lfloor m(1 - \sin \alpha) / \cos \alpha \rfloor$ layer of SLM pixels to zero.

Before beginning with the algorithm, we need to first estimate the angle of rotation. By sending a known preamble of pixel pattern and measuring the detected signal at a predestinated location we can estimate the angle of rotation. This measurement is used subsequently in the reconstruction algorithm. As an illustration, consider Figure 6. By presetting the transmitted SLM array as an all zero pattern except at location $(1,1)$ and by measuring the detected signals $d(1,2), d(1,1)$, we can estimate the angle of rotation.

We assume that the SLM and CCD fill factors are low so that we can get rid of the integrals in equations (6). The integrands will be evaluated at the center of the detector pixel. We can take the square root of the detected signal and do linear processing for signal recovery. With the above framework, we will now outline an algorithm for signal recovery.

The recovery process is done in two blocks. The first block comprises of all the detector pixels towards the right half plane of the detector array. The second block consists of all pixels in the left half plane.

For the first block, detector pixels are sequentially scanned starting from the top most row until all the transmitted SLM bits are sequentially decoded from right to left

along this row. The scanner moves to the next row and repeats the process of decoding all the row bits before starting the next row. This process iterates until all the bits in the first block are decoded. The idea is illustrated in Figure 9. For the second block the scanner starts from the bottom most row in the left half plane, decodes all the bits from left to right along that row, moves to next top row and iterates the process till all the bits are recovered.

We can also do the decoding by processing the array of detected signals in four blocks corresponding to each of the four quadrants and then average the results obtained from the two block scanning and decoding process illustrated in Figure 9. This averaging technique will be helpful especially in the presence of severe detector noise when the decoding errors tend to propagate.

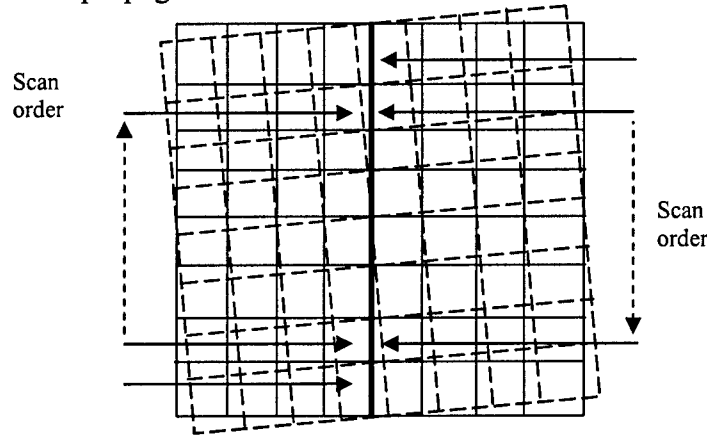


Figure 9: Scanning and decoding process

We now outline the steps for the decoding of the first block in the form of an algorithm described below. The decoding algorithm for the second block follows anti symmetrically in exactly the same way as the first block.

Outline of the Algorithm

Introduce the following definitions:

s : Array representing the decoded bits.

d : Array holding the detected signal values.

Initialize:

- Set all the pixels of the array s along the rows from $\lfloor m(1 - \sin \alpha) / \cos \alpha \rfloor$ to m as zero. Also set all the pixels of the array s from columns $\lfloor m(1 - \sin \alpha) / \cos \alpha \rfloor$ to m as zero.

Algorithm Steps

Set the detector index to the top right corner $(r, c) = (m, m)$

1. Obtain the SLM pixel indices that overlap with (r, c) as $(a, b), (a-1, b), (a, b-1)$ and $(a-1, b-1)$ where $(a, b) = \lceil r \cos \alpha + c \sin \alpha \rceil \lceil -r \sin \alpha + c \cos \alpha \rceil$.
2. Evaluate the components of the kernel $g_{a-1,b}(x, y), g_{a,b}(x, y)$ and $g_{a,b-1}(x, y)$ at the center of the detector pixel $x = r - 0.5, y = c - 0.5$.
3. Obtain the component of the signal energy for SLM pixel $(a-1, b-1)$ as $\sqrt{d(r, c)} - q$ where, $q = g_{a,b}\sqrt{s(a, b)} - g_{a-1,b}\sqrt{s(a-1, b)} - g_{a,b-1}\sqrt{s(a, b-1)}$
4. Compute $\left(\frac{\sqrt{d(r, c)} - q}{g_{a-1,b-1}(r - 0.5, c - 0.5)} \right)^2$.
5. If $\left(\frac{\sqrt{d(r, c)} - q}{g_{a-1,b-1}(r - 0.5, c - 0.5)} \right)^2 > 0.5$, decode $s(a-1, b-1) = 1$. Else decode $s(a-1, b-1) = 0$.
6. $c \leftarrow c - 1$. Loop back to Step 2 till $c = 1$.
7. $r \leftarrow r - 1$. Loop back to Step 2 till $r = -m + 2$

It is interesting to note that the decoding process is simple and the algorithm has no extra storage overheads. The time complexity of the algorithm is linear in the number of pixels decoded. We use threshold detection at Step 6 to circumvent round off errors and for handling detector noise.

To test the performance of the algorithm, several pages of 100x100 pixel arrays were modeled to mimic the detector output with 3 degrees rotational misalignment. White Gaussian noise was added to the detector output. The noise variance was varied to obtain the different SNRs. Table 4 shows the average bit error rate (BER) versus signal to noise ratio (SNR). It is interesting to note that the decoding algorithm performs well with high SNR and is fairly robust with SNRs around 30-40dB intended for practical scenarios.

SNR (dB)	BER
∞	0
60	0.001
20	0.25
10	0.4034

Table 4: SNR versus BER results

The misalignment induced inter-pixel interference can be interpreted as reduction of SNR in the optical domain proportional to the amount of overlap between the SLM and detector.

6. On going Research Areas

There are several new thrusts to research problems in two-dimensional coding and signal processing some of which find applications in futuristic optical CDMA communications and information processing along two-dimensional plane wave medium.

- In certain communication systems like optical storage devices and optical CDMA applications, there is a need for developing codes that are balanced. Such constraints are called *dc free* constraints. Designing higher order spectral null codes is one of the issues that we are looking into.
- Another research line is that of two-dimensional error correcting codes. It might be worth noting that the codes we have developed have some redundancy dictated in some way by the capacity estimates. The loss of rate combined with good hamming distance properties can help in building codes that are resilient to burst errors common on optical disks. Thus combined modulation as well as error correction makes this an attractive feature than having two separate codes for increased data storage and error protection. We are investigating into some aspects of two-dimensional interleaving and error correcting codes.
- From the signal-processing standpoint, we are also looking at capacity issues for two-dimensional ISI channels and equalization techniques for the same.

7. Conclusions

We presented coding schemes and capacity estimates for a class of $(d_1, \infty, d_2, \infty)$ RLL constraints. Some of the 2-D bounding techniques developed here also solve the 1-D constrained coding problem in a constructive way. We can easily extend the combinatorial bounds presented in this report for M-ary 2-D RLL optical storage that might be of future research interest. We also provided an analysis of the channel model for misregistration and sketched an outline of the signal-processing algorithm.

From an information theoretic perspective, we need a general theory for capacity analysis of 2-D RLL channels. Also a computable formula in closed form is rather preferred to numerical bounds. An exact analysis for the theory behind 2-D constrained systems will be a seminal contribution to the field of pure mathematics.

In the signal processing front, we developed a model for handling misregistration. The model is applicable to a general optical communications setup where the transmitted signal suffers from the misregistration artifacts. Noise robust 2-D adaptive algorithms, which are fundamentally non-linear, need to be investigated for recursively estimating and recovering the 2-D signal.

References

- [1] C.E.Shannon, "A Mathematical Theory of Communication," in *Bell Syst. Tech. J.*, no.27, pp. 379-423 (part I) and pp. 623-656 (part II), 1948.
- [2] N.J.Calkin and H.S.Wilf, "The Number of Independent Sets in a Grid Graph," in *SIAM J.Disc.Math.*, vol.11, pp. 54-60, Feb. 1998.
- [3] S. Srinivasa and S.McLaughlin, "Enumeration Algorithms for Constructing $(d_1, \infty, d_2, \infty)$ RLL Arrays: Capacity Estimates and Coding Schemes," in *IEEE Information Theory Workshop*, TX, 2004.
- [4] S. G. Srinivasa and S. W. McLaughlin, "Algorithms for Constructing a Class of $(1, \infty, d, k)$ Run Length Limited Constraints and Capacity Estimates," in *Univ. Illinois* press, 41st Allerton Conference on Computing, Communication and Control, Monticello, IL 2003.
- [5] G.W.Burr and T.Weiss, "Compensation for Pixel-Misregistration in Volume Holographic Data Storage," in *Optics Letters.*, vol.26, pp. 542-544, April 2001.
- [6] S. Halevy, J. Chen, R. M. Roth, P. H. Siegel and J. K. Wolf, "Improved Bit-stuffing Bounds on Two-Dimensional Constraints," *IEEE Int. Symp. Inform. Theory.*, Sorrento, Italy, pp. 285, Aug. 2002.
- [7] D. Lind and B. H. Marcus, "An Introduction to Symbolic Dynamics and Coding," *New York: Cambridge Univ. Press*, 1995.
- [8] A. Kato and K. Zeger, "On the Capacity of Two-Dimensional Run-Length Constrained Channels," *IEEE Trans. Inform. Theory.*, vol.45, pp. 1527-1540, July. 1999.
- [9] R. M. Roth, P. H. Siegel and J. K. Wolf, "Efficient Coding Schemes for the Hard-Square Model," *IEEE Trans. Inform. Theory.*, vol.47, pp. 1166-1176, March. 2001.
- [10] S. G. Srinivasa and S.McLaughlin, "Signal Recovery due to Rotational Pixel Misalignment," to appear in *IEEE International Conference on Acoustics Speech and Signal Processing*, Philadelphia, MA 2005.
- [11] H.J. Coufal, D.Psaltis, and G. Sincerbox, eds. *Holographic Data Storage*, Springer-Verlag, NewYork, 2000.

REPORT DOCUMENTATION PAGE

AFRL-SR-AR-TR-05-

Public reporting burden for this collection of information is estimated to average 1 hour per response, including the time for reviewing existing information, gathering and maintaining the data needed, and completing and reviewing the collection of information. Send comments regarding this burden estimate or any other aspect of this collection of information, including suggestions for reducing this burden, to Washington Headquarters Services, Directorate for Information Operations and Reports, 1215 Jefferson Davis Highway, Suite 1204, Arlington, VA 22202-4302, and to the Office of Management and Budget, Paperwork Reduction Project (0707-0188), Washington, DC 20503.

02 58

1. AGENCY USE ONLY (Leave blank)	2. REPORT DATE	3. REPORT TYPE AND DATES COVERED 01 Dec 2001 - 30 Nov 2004 FINAL	
4. TITLE AND SUBTITLE ULTRA-HIGH CAPACITY HOLOGRAPHIC MEMORIES		5. FUNDING NUMBERS 61102F 2305/HX	
6. AUTHOR(S) DR ADIBI			
7. PERFORMING ORGANIZATION NAME(S) AND ADDRESS(ES) GEORGIA INSTITUTE OF TECHNOLOGY GEORGIA TECH RESEARCH CORP ATLANTA GA 30332-0415		8. PERFORMING ORGANIZATION REPORT NUMBER	
9. SPONSORING/MONITORING AGENCY NAME(S) AND ADDRESS(ES) AFOSR/NE 4015 WILSON BLVD SUITE 713 ARLINGTON VA 22203		10. SPONSORING/MONITORING AGENCY REPORT NUMBER F49620-02-1-0053	
11. SUPPLEMENTARY NOTES			
12a. DISTRIBUTION AVAILABILITY STATEMENT DISTRIBUTION STATEMENT A: Unlimited		12b. DISTRIBUTION CODE	
13. ABSTRACT (Maximum 200 words) During the 3-year period of the program, extensive progress has been made in all three thrusts. The development of a complete model for global optimization of doubly-doped photorefractive crystals, especially lithium niobate (LiNbO ₃), experimental demonstration of recording high dynamic range and sensitivity in LiNbO ₃ :Fe:Mn crystals, the development of a stabilized holographic read/write setup, the development of a fully two-dimensional low-density parity-check (LDPC) code optimized for holographic memories, and the implementation of new approaches for the incorporation of novel signal processing techniques into holographic memory systems, are the major achievements in this period. Currently, we are in the process of setting up a complete testbed for these volume holographic memory modules. The final goal of the demonstration of a persistent Holographic memory system (both hardware and software) for digital data storage for the first time will be achieved in next few months.			
14. SUBJECT TERMS		15. NUMBER OF PAGES	
		16. PRICE CODE	
17. SECURITY CLASSIFICATION OF REPORT Unclassified	18. SECURITY CLASSIFICATION OF THIS PAGE Unclassified	19. SECURITY CLASSIFICATION OF ABSTRACT Unclassified	20. LIMITATION OF ABSTRACT UL

7-7-05